Key Points:
- The neuro-fuzzy kinematic finite-fault inversion used to study the Amatrice earthquake; We compare the inferred slip with previous studies
- We present a new maximum-likelihood strategy to select an adequate, problem-specific number of fuzzy basis functions
- The inferred source model is able to correctly predict high-rate GNSS waveforms not used in the inversion

Supporting Information:
Supporting Information may be found in the online version of this article.

Correspondence to:
A. Ansari,
a.ansari@iiees.ac.ir

Neuro-Fuzzy Kinematic Finite-Fault Inversion: 2. Application to the Mw6.2, August/24/2016, Amatrice Earthquake

Navid Kheirdast[1] [iD], **Anooshiravan Ansari[1]** [iD], **and Susana Custódio[2]** [iD]

[1]International Institute of Earthquake Engineering and Seismology (IIEES), Tehran, Iran, [2]Instituto Dom Luiz (IDL), Faculdade de Ciências, Universidade de Lisboa, Lisbon, Portugal

Abstract In this article, we validate the neuro-fuzzy kinematic finite-fault inversion method by studying the rupture process of the M_w 6.2, Aug/24/2016, Amatrice, central Italy, earthquake. We jointly invert three different datasets to infer the spatio-temporal slip distribution, namely static and high-rate GNSS data ($<= 0.06$ Hz) and strong-motion data ($0.06 - 0.5$ Hz). Each data set is used to constrain a different frequency range of the source model, depending on the sensitivity of the data set. The inferred slip shows a slow nucleation phase at shallow depths of 3–4 km, followed by a bilateral rupture that forms two asperities, one to the NW (Norcia) and another to the SE (Amatrice) of the hypocenter. Our inferred slip is compared with those previously obtained using well-established methods. In order to select an adequate number of fuzzy basis functions, we propose two alternative procedures, which yield the same general slip features. The first approach consists of ensuring that the inverse problem is formally over-determined and uses the same number of basis functions at all frequencies. The second approach is based on a maximum-likelihood analysis of the model misfit and selects a different number of basis functions for each frequency. The maximum-likelihood approach allows for more basis functions at high frequencies, where more detail in the spatial slip distribution is needed. The solution obtained with the maximum-likelihood approach provides a more physically plausible source time function, which shows less back slip artifacts. The accurate prediction of high-rate GNSS traces not used in the inversion attests the robustness of the inferred slip model.

Plain Language Summary The accuracy of the earthquake's slip imaging method proposed in the companion article by Kheirdast et al. (accepted), is tested using data recorded during the 2016 M_w 6.2, Amatrice, earthquake. Many previously well-understood features of the rupture process of this earthquake are well retrieved by the proposed method, including a slow nucleation phase, a bilateral rupture and a high-amplitude slip patch to the NW of the hypocenter. We present a new strategy to spatially discretize the fault plane, which maximizes the inversion power by taking into account the uncertainty at different frequencies.

1. Introduction

In the companion article by Kheirdast et al. (accepted), we introduced a new kinematic finite-fault method based on a fuzzy function approximation approach. The neuro-fuzzy inversion aims to improve the robustness of the slip solutions by reducing the number of basis functions that spatially describe the slip function at each frequency and optimizing the approximation parameters using the learning techniques of neural networks. In the proposed methodology, the inversion is carried out in the frequency domain.

In the companion article, the method was tested using synthetic data from the benchmark exercise SIV1 of the the Earthquake-Source Inversion Validation community (Mai et al., 2016). In this article, we further validate the new neuro-fuzzy finite-fault inversion method by applying it to data of the M_w 6.2 Amatrice earthquake. This earthquake was extremely well recorded and its source mechanism has been characterized in detail by several authors (e.g., Aochi & Twardzik, 2019; Cheloni et al., 2017; Cirella et al., 2018; Gallovič et al., 2019b; Huang et al., 2017; Magnoni & Casarotti, 2016; Pizzi et al., 2017; Ragon et al., 2019; Tinti et al., 2016).

The Amatrice earthquake occurred on August/24/2016 in central Italy. It was assigned a magnitude M_w 6.2 by the Global CMT Project (Ekstrom et al., 2012) and M_w 6.0 by INGV, Italy (http://terremoti.ingv.it/en/event/7073641). The earthquake was relatively shallow, with the hypocenter located at a depth of ~ 8 km below the surface (Chiaraluce et al., 2017). Ground shaking was strongly felt in the towns of Amatrice and Norcia, located approximately 10 km to the SE and 15 km to the NW of the epicenter, respectively. The earthquake caused ~ 300 fatalities. Its epicenter was located approximately 40 km NW of L'Aquila, a nearby region that had been previously hit in 2009 by a M_w 6.3 earthquake (Chiaraluce et al., 2017). The M_w 6.2 Amatrice event occurred within a complex earthquake sequence that included numerous aftershocks and another two earthquakes with magnitude larger than 6: The M_w 6.1 Ussita earthquake on 26/October/2016 and the M_w 6.5 Norcia earthquake on Oct/30/2016 (Chiaraluce et al., 2017; Pizzi et al., 2017; Scognamiglio et al., 2018). All three events with magnitude larger than 6 (Amatrice, Ussita and Norcia) had a normal focal mechanism, in good agreement with the dominant extensive faulting regime of the Central Apennines (Pizzi et al., 2017). The Amatrice mainshock was very well recorded, generating a rich data set that includes, amongst others, openly available strong-motion accelerograms (Luzi, Puglia, Russo, D'Amico, et al., 2016; Luzi, Puglia, Russo, & ORFEUS WG5, 2016) and both static and high-rate GNSS observations (Avallone et al., 2016; Cheloni et al., 2017) (Figure 1).

A rapid finite-fault inversion of strong-motion data suggested that the Amatrice earthquake consisted of a bilateral rupture, propagating to both ends of the fault from the nucleation point (Tinti et al., 2016). The cumulative slip distribution showed two asperities, one to either side of the hypocenter. Geodetic InSAR observations from ALOS-2 and Sentinel-1 also showed the existence of two distinct patches of surface displacement above the fault plane, one to the NW and the other to the SE of the epicenter, in good agreement with the double asperity proposed by finite-fault models (Cheloni et al., 2017; Huang et al., 2017; Lavecchia et al., 2016; Walters et al., 2018). More advanced inversions based on 3D finite element modeling of ALOS-2 InSAR data allowed to compare the slip distributions obtained under the assumptions of a planar versus listric fault (Tung & Masterlark, 2018). The authors concluded that a planar fault allows to model well the Amatrice earthquake. The kinematic source time functions of the M_w 6.2 Amatrice, M_w 6.1 Ussita and M_w 6.5 Norcia earthquakes were investigated by Pizzi et al. (2017) using the method of Gallovič et al. (2015). The authors proposed that the Miocene-Pliocene Sibillini Mts. thrust fault, which intersects active faults in the region, acted as a structural barrier to the propagation of slip. These results were confirmed by Scognamiglio et al. (2018), who showed that the slip surface of the M_w 6.5 Norcia earthquake is composed of two conjugate surfaces, a major segment interfacing between the Mt. Vettore-Mt. Bove (VBFS) and Laga Mts. (LMFS) fault systems and a minor segment located on the Sibillini Mts. fault system, which intersects the major plane. The Sibillini Mts. fault system partitions the loading rate on fault systems located on its two sides, controlling the activation of individual segments during the Amatrice and Ussita earthquakes, that is, during the first two M6+ earthquakes of the sequence (Pizzi et al., 2017; Scognamiglio et al., 2018). Aochi and Twardzik (2019) used a hybrid method based on the boundary integral equation and on finite differences to simulate the dynamic rupture of the resulting wavefield. The rupture parameters were searched using an iterative methodology. Gallovič et al. (2019b) applied a novel Bayesian inversion in order to find the best fitting dynamic rupture parameters of the earthquake, namely the initial stress throughout the fault (τ_i), the difference between static and dynamic friction coefficients ($\mu_s - \mu_d$) and the characteristic slip-weakening distance (D_c).

Several methods of finite-fault inversion have been proposed over the past 40 years, since the pioneering work of Olson and Apsel (1982) (for brief reviews, we refer the reader to Mai et al. (2016) and to the companion article by Kheirdast et al. (2021)). An inherent difficulty of kinematic finite-fault inversions arises from the ill-posedness of the Fredholm integral of the first kind in the representation theorem of seismology. This forward equation, which allows to compute ground motion from given a slip model, can be formulated either in the time (e.g., Das & Kostrov, 1990; Gallovič & Zahradník, 2011; Gallovič et al., 2015; Hartzell & Heaton, 1983; Liu & Archuleta, 2004; Olson & Apsel, 1982) or frequency domain (e.g., Cotton & Campillo, 1995; Fan et al., 2014; Olson & Anderson, 1988). In the neuro-fuzzy method, we followed the frequency domain formulation proposed by Fan et al. (2014). Thus, we search for the best source function independently for each frequency. At each frequency, a spatial slip distribution is approximated using an Adaptive Neuro-Fuzzy Inference System (ANFIS). Some of the main advantages of the neuro-fuzzy
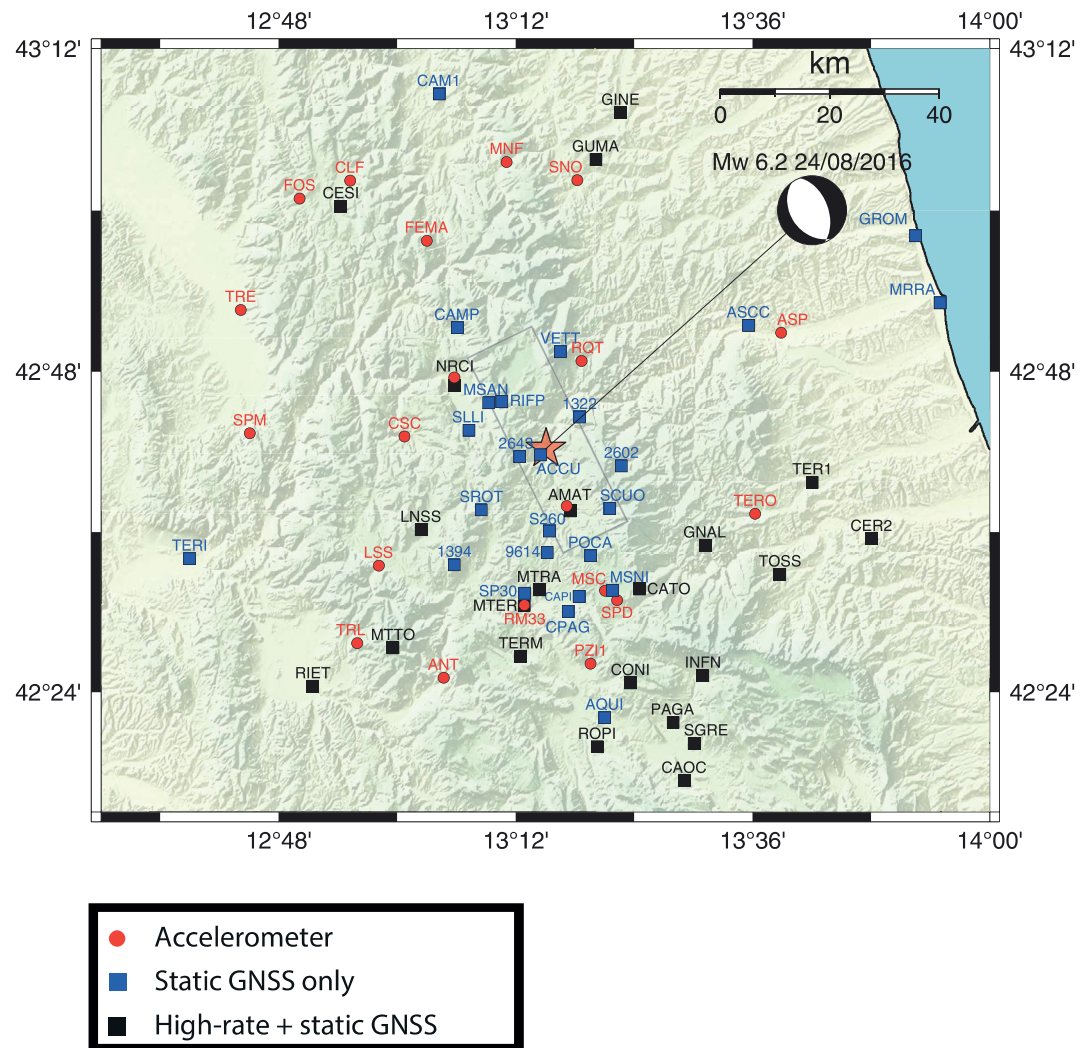
Figure 1. Epicentral region of the August/24/2016 Amatrice, central Italy, earthquake. The data used in this study consist of near-fault (<60 km) GNSS displacements (squares) and strong-motion records (circles). Of the 47 GNSS stations, 22 are equipped with high-rate sensors (black squares) and the remaining 25 stations provide only static deformation (blue squares). The red circles mark the 20 accelerometers whose data is available on the ESM database (Luzi, Puglia, Russo, & ORFEUS WG5, 2016). In order to compare the results of the fuzzy inversion method with previous studies, we selected the same strong-motion data set as used by Gallovič et al. (2019b); Pizzi et al. (2017). The epicenter of the mainshock is marked by the red star (Chiaraluce et al., 2017). The beachball on the top right corner indicates a normal earthquake on a fault striking NW-SE (http://terremoti.ingv.it/en/event/7073641).

finite-fault inversion method are: A low number of basis functions could be used to solve the inverse problem at each frequency, which reduces the ill-posedness of the inverse problem; the use of C^∞ basis functions to estimate slip, which allows the generation of high-quality synthetic ground motion; and the use of different sets of points for integration and regularization, which renders the problem more stable. The fact that the inversion is carried out in the frequency domain can also be advantageous. In particular when different datasets that are sensitive to ground motion at different frequencies are combined in a single inversion, the frequency domain approach allows for a natural way to integrate the various datasets. For example, InSAR data provides a high-resolution, spatially dense image of the surface displacement caused by an earthquake. However, because InSAR data only captures the static field, it can only be used to constrain the static slip distribution, that is, slip at $f \approx 0$ Hz. The same is true for campaign GNSS data. On the other hand, continuous high-rate GNSS sensors can sample ground motion from the static $f \approx 0$ Hz component up to the Nyquist frequency, which – as an example – would be 0.5 Hz for data sampled at 1 Hz. On the other hand,

broadband stations and accelerometers are designed to capture the dynamic wavefield, so they are sensitive to high-frequency ground motion (>0.01 Hz), which is key to infer the physics of seismic sources. However, the sensitivity of seismic data to low-frequency ground motion, including the static field, is limited.

In this work, we used static GNSS displacements recorded at 47 stations near the Amatrice earthquake (epicentral distances < 60 km) (Cheloni et al., 2017) to constrain the static ($f = 0$ Hz) slip distribution. We then used high-rate GNSS displacement waveforms recorded at 22 near-field stations (Avallone et al., 2016) to constrain the slip distribution at low frequencies, namely at frequencies ranging between 0.03 and 0.06 Hz. Finally, in the frequency range $0.06\,\text{Hz} - 0.5\,\text{Hz}$, the slip distribution was constrained by strong-motion data only. The main aim of this article is to assess the performance of the neuro-fuzzy finite-fault inversion method by applying it to the study of a real earthquake. In order to easily compare our results with those of previous studies, we used the same strong-motion data as used by Gallovič et al. (2019b); Pizzi et al. (2017) and we did not include high-rate GNSS data in the inversion. Therefore, the robustness of the solution can be assessed by comparing GNSS waveforms not used in the inversion with synthetic waveforms predicted by our final model in the high frequency range ($0.06\,\text{Hz} - 0.5\,\text{Hz}$).

In this article, we first develop the preliminary model-space parameterization, such that it considers slip both in the along-strike and updip directions (Section 2). After introducing the data (Section 3) and setting up the inversion parameters (Section 4), we present the inversion results (Section 5). In Section 6, we introduce a new approach to determine the number of adequate fuzzy membership functions at each frequency. To this end, we carry out inversions with a variable number of basis functions and compute the likelihood of the misfit values. In Section 7.1, we compare our results with those obtained by selected previous studies (Aochi & Twardzik, 2019; Gallovič et al., 2019b; Pizzi et al., 2017). We finally discuss the back slip artifact in the inverted slip-rate functions (Section 7.2) and evaluate the accuracy of the solutions obtained in the frequency range $0.06\,\text{Hz} - 0.5\,\text{Hz}$ using high-rate GNSS traces as a validation data set (Section 7.4).

2. Generalization of the Neuro-Fuzzy Kinematic Finite-Fault Method to Slip With Arbitrary Rake

2.1. The Forward Problem

In the companion article, for the sake of simplicity, we presented the neuro-fuzzy kinematic finite-fault method considering that slip on the fault occurred only in the along-strike direction (Kheirdast et al., 2021). In other words, we assumed that the earthquake was purely strike-slip. However, in most real applications, slip can have an arbitrary rake angle. Therefore, the slip vector must be defined by two components: One along strike and the other up dip on the fault plane. We can easily generalize the methodology presented in the companion article by considering a general slip vector **u** with two orthogonal components. Throughout this article we follow the same notation as in the companion article (Kheirdast et al., 2021). As before, slip on the fault varies with location on the fault along-strike (ξ), updip (η) and with the frequency considered (ω):

$$\mathbf{u}(\xi,\eta,\omega) = \mathbf{v}_s u_s(\xi,\eta,\omega) + \mathbf{v}_d u_d(\xi,\eta,\omega), \tag{1}$$

where $\mathbf{v}_s$ and $\mathbf{v}_d$ are the two independent orthogonal normalized unit vectors, along-strike and updip, respectively, and u_s and u_d are the amplitudes of slip along the two directions. Note that we will need to use two independent Adaptive Network–based Fuzzy Inference Systems (ANFIS) in order to reconstruct u_s and u_d at each frequency ω_j:

$$u_s(\xi,\eta,\omega_j) = \sum_{i\xi=1}^{N_\xi} \sum_{i\eta=1}^{N_\eta} \overline{W}_{s,i\xi,i\eta,\omega_j}(\xi,\eta) A_{s,i\xi,i\eta,\omega_j} \tag{2}$$

$$u_d(\xi,\eta,\omega_j) = \sum_{i\xi=1}^{N_\xi} \sum_{i\eta=1}^{N_\eta} \overline{W}_{d,i\xi,i\eta,\omega_j}(\xi,\eta) A_{d,i\xi,i\eta,\omega_j}, \tag{3}$$

where $\bar{W}_{s,i\xi,i\eta,\omega_j}$ and $\bar{W}_{d,i\xi,i\eta,\omega_j}$ represent the fuzzy basis functions for the u_s and u_d components of slip, respectively, and $A_{s,i\xi,i\eta,\omega_j}$ and $A_{d,i\xi,i\eta,\omega_j}$ are their amplitudes. Following our methodology, the basis functions of slip ($\bar{W}_{s,i\xi,i\eta,\omega_j}$ and $\bar{W}_{d,i\xi,i\eta,\omega_j}$) are based on Gaussian membership functions (*gmf*) (see Equation 6 in Kheirdast et al., 2021).

Next, we write the representation theorem, which allows us to describe ground motion, $u_n^o(\mathbf{x},\omega)$, as a function of slip on the fault:

$$\begin{aligned} u_n^o(\mathbf{x},\omega) &= \int_\Sigma \left(v_{si} u_s(\xi,\eta,\omega) + v_{di} u_d(\xi,\eta,\omega) \right) c_{ijpq} v_j \frac{\partial}{\partial(\xi_q)} G_{np}(\mathbf{x};\xi,\eta,\omega) d\Sigma \\ &= \int_\Sigma u_s(\xi,\eta,\omega) v_{si} c_{ijpq} v_j \frac{\partial}{\partial(\xi_q)} G_{np}(\mathbf{x};\xi,\eta,\omega) d\Sigma \\ &+ \int_\Sigma u_d(\xi,\eta,\omega) v_{di} c_{ijpq} v_j \frac{\partial}{\partial(\xi_q)} G_{np}(\mathbf{x};\xi,\eta,\omega) d\Sigma \end{aligned} \tag{4}$$

where we introduced the Green's functions, $G_{np}(\mathbf{x};\xi,\eta,\omega)$ (see Kheirdast et al., 2021, for details on the notation). Next, we separate the Green's functions into the components that result from updip and along-strike slip:

$$G'_{sn} = v_{si} c_{ijpq} v_j \frac{\partial}{\partial(\xi_q)} G_{np} \tag{5}$$

$$G'_{dn} = v_{di} c_{ijpq} v_j \frac{\partial}{\partial(\xi_q)} G_{np} \tag{6}$$

By replacing the Green's functions (Equations 5 and 6) in the forward relationship (Equation 4), the latter becomes:

$$u_n^o(\mathbf{x},\omega_j) = \int_\Sigma u_s(\xi,\eta,\omega_j) G'_{sn}(\mathbf{x};\xi,\eta,\omega_j) d\Sigma + \int_\Sigma u_d(\xi,\eta,\omega_j) G'_{dn}(\mathbf{x};\xi,\eta,\omega_j) d\Sigma. \tag{7}$$

We now replace the fuzzy approximation for slip on the fault, u_s and u_d (Equations 2 and 3), in the representation theorem (Equation 7):

$$u_n^o(\mathbf{x},\omega_j) = \left(\underbrace{\sum_{i\xi=1}^{N_\xi} \sum_{i\eta=1}^{N_\eta} \int_\Sigma \bar{W}_{s,i\xi,i\eta,\omega_j}(\xi,\eta) G'_{sn}(\mathbf{x};\xi,\eta,\omega_j) d\Sigma}_{(\mathbf{GW})_{s,\omega_j}} \right) A_{s,i\xi,i\eta,\omega_j} + \left(\underbrace{\sum_{i\xi=1}^{N_\xi} \sum_{i\eta=1}^{N_\eta} \int_\Sigma \bar{W}_{d,i\xi,i\eta,\omega_j}(\xi,\eta) G'_{dn}(\mathbf{x};\xi,\eta,\omega_j) d\Sigma}_{(\mathbf{GW})_{d,\omega_j}} \right) A_{d,i\xi,i\eta,\omega_j} \tag{8}$$

This forward relationship (Equation 8) can be easily represented in matrix form, for each frequency:

$$\mathbf{d}_{\omega_j} = (\mathbf{GW})_{s,\omega_j} \mathbf{A}_{s,\omega_j} + (\mathbf{GW})_{d,\omega_j} \mathbf{A}_{d,\omega_j} = \begin{bmatrix} (\mathbf{GW})_{s,\omega_j} & (\mathbf{GW})_{d,\omega_j} \end{bmatrix} \begin{bmatrix} \mathbf{A}_{s,\omega_j} \\ \mathbf{A}_{d,\omega_j} \end{bmatrix} \tag{9}$$

2.2. Regularization and Inversion

The forward Equation 9 allows the modeling of seismic waveforms at different stations given a known slip distribution, which is expressed in terms of fuzzy basis fuctions, $\bar{W}_{s,i\xi,i\eta,\omega_j}$ and $\bar{W}_{d,i\xi,i\eta,\omega_j}$, and their respective amplitudes, $\mathbf{A}_{s,\omega_j}$ and $\mathbf{A}_{d,\omega_j}$. In order to avoid ill-posedness when inverting for the slip model from observed ground-motion, we follow the same approach as outlined in the companion article and apply a regularizing constraint (Kheirdast et al., 2021). We require slip to vary in a spatially smooth manner, both along-strike and updip. Thus, we optimize two conditions during the inversion: (a) good fit between data and synthetics, and (b) minimization of the Laplacian ($\mathbf{L}$) of the slip distribution:

$$\begin{aligned}
&\left\| \begin{bmatrix} (\mathbf{GW})_{s,\omega_j} & (\mathbf{GW})_{d,\omega_j} \end{bmatrix} \begin{bmatrix} \mathbf{A}_{s,\omega_j} \\ \mathbf{A}_{d,\omega_j} \end{bmatrix} - \mathbf{d}_{\omega_j}^o \right\|_2 < \delta \\
\min \quad &\left\| \mathbf{L} \begin{bmatrix} \mathbf{W}_{s,\omega_j} & \mathbf{W}_{d,\omega_j} \end{bmatrix} \begin{bmatrix} \mathbf{A}_{s,\omega_j} \\ \mathbf{A}_{d,\omega_j} \end{bmatrix} \right\|_2
\end{aligned} \tag{10}$$

The solution to Equation 10 can easily be found by classical Tikhonov regularization (Hansen, 2005), where we introduce the regularizing parameter α:

$$\min \left\| \begin{bmatrix} (\mathbf{GW})_{s,\omega_j} & (\mathbf{GW})_{d,\omega_j} \\ \alpha \mathbf{LW}_{s,\omega_j} & \alpha \mathbf{LW}_{d,\omega_j} \end{bmatrix} \begin{bmatrix} \mathbf{A}_{s,\omega_j} \\ \mathbf{A}_{d,\omega_j} \end{bmatrix} - \begin{bmatrix} \mathbf{d}_{\omega_j} \\ \mathbf{0} \end{bmatrix} \right\|_2^2 \tag{11}$$

Note that the parameter α represents the weight given to smoothness with respect to data fit. As explained in the companion article, the damping parameter α can be found using L-curve diagrams, which determine the optimal trade-off between data fit and slip smoothness.

If the fuzzy basis functions ($\mathbf{W}_{\omega_j}$) are known, then the respective amplitudes ($\mathbf{A}_{\omega_j}$) can be found by simple least squares linear inversion:

$$\left(\begin{bmatrix} (\mathbf{GW})_{s,\omega_j} & (\mathbf{GW})_{d,\omega_j} \end{bmatrix}^T \begin{bmatrix} (\mathbf{GW})_{s,\omega_j} & (\mathbf{GW})_{d,\omega_j} \end{bmatrix} + \tag{12}$$

$$\alpha^2 \begin{bmatrix} \mathbf{LW}_{s,\omega_j} & \mathbf{LW}_{d,\omega_j} \end{bmatrix}^T \begin{bmatrix} \mathbf{LW}_{s,\omega_j} & \mathbf{LW}_{d,\omega_j} \end{bmatrix} \right) \begin{bmatrix} \mathbf{A}_{s,\omega_j} \\ \mathbf{A}_{d,\omega_j} \end{bmatrix} = \begin{bmatrix} (\mathbf{GW})_{s,\omega_j} & (\mathbf{GW})_{d,\omega_j} \end{bmatrix}^T \mathbf{d}_{\omega_j}$$

In order to find both the optimal fuzzy basis functions and their amplitudes, we use a hybrid inversion scheme, which iterates between optimizing the fuzzy basis functions ($\mathbf{W}_{\omega_j}$) by gradient descent (non-linear step) and optimizing the amplitudes of the basis functions ($\mathbf{A}_{\omega_j}$) by linear least squares (linear step) (Kheirdast et al., 2021). Accordingly, the cost function to be minimized during hybrid learning is:

$$Cost_{FIM} = \underbrace{\left\| \begin{bmatrix} (\mathbf{GW})_{s,\omega_j} & (\mathbf{GW})_{d,\omega_j} \end{bmatrix} \begin{bmatrix} \mathbf{A}_{s,\omega_j} \\ \mathbf{A}_{d,\omega_j} \end{bmatrix} - \mathbf{d}_{\omega_j} \right\|_2^2}_{Cost_{data}} + \alpha^2 \underbrace{\left\| \begin{bmatrix} \mathbf{LW}_{s,\omega_j} & \mathbf{LW}_{d,\omega_j} \end{bmatrix} \begin{bmatrix} \mathbf{A}_{s,\omega_j} \\ \mathbf{A}_{d,\omega_j} \end{bmatrix} \right\|_2^2}_{Cost_{smooth}} \tag{13}$$

The hybrid learning scheme iterates between the linear and nonlinear steps, where the linear step aims to find the slip amplitudes $\mathbf{A}_{s,\omega_j}$ and $\mathbf{A}_{d,\omega_j}$ from the normal equation (Equation 12) and the nonlinear step aims to minimize $Cost_{FIM}$ (Equation 13) by optimizing the non-linear parameters that define the slip basis functions (μ and σ, which respectively represent the center and spread of the Gaussian membership functions) using gradient descent method. After enough learning epochs, the solution arrives at a stationary point, indicating that a suitable slip model was found.

3. Data and Velocity-Density-Attenuation Model

We used three ground-motion datasets that are openly available: (a) static GNSS displacements, (b) high-rate GNSS (HR-GNSS) displacement waveforms, and (c) strong-motion accelerograms. As mentioned in Section 1, each of these datasets is sensitive to a different frequency range of ground motion. Accordingly, we used: (a) static GNSS displacements to constrain the static, f = 0Hz, slip distribution; (b) high-rate GNSS displacement waveforms to constrain slip between 0.03 and 0.06 Hz; and (c) strong-motion data to constrain the slip model at frequencies between 0.06 and 0.5 Hz.

A dense static GNSS data set was obtained from Cheloni et al. (2017). High-rate GNSS displacements were taken from Avallone et al. (2016). The authors processed raw GNSS observations acquired by several GNSS networks, including RING (INGV Ring Working Group and others, 2016) (http://ring.gm.ingv.it/), INGV CaGeoNet (Galvani et al., 2013), ISPRA (https://www.isprambiente.gov.it/), Regione Lazio (http://

Table 1
Layered (1D) Density-Velocity-Attenuation Model for the L'Aquila Region (Ameri et al., 2012)

Thickness (m)	$V_p(\frac{m}{s})$	$V_s(\frac{m}{s})$	Density ($\frac{kg}{m^3}$)	Q_p	Q_s
1000.	3160.	1700.	2500	200	100
1000.	4830.	2600.	2840.	400	200
3000.	5760.	3100.	2940.	400	200
22,000.	6510.	3500.	3150.	400	200
15,000.	7000.	3800.	3260.	600	300
18,000.	7800.	4200.	3500.	800	400

gnss-regionelazio.dyndns.org/Spiderweb/frmIndex.aspx), Regione Abruzzo (http://gnssnet.regione.abruzzo.it/), ITALPOS (http://it.smart-net-eu.com/) and NATGEO (http://www.netgeo.it/). The high-rate GNSS time-series have variable sampling intervals of 0.05, 0.1, 0.5 and 1 s, depending on station, which correspond to Nyquist frequencies of 10 Hz, 5 Hz, 1 Hz and 0.5 Hz, respectively.

Strong-motion data was recorded by two networks, namely by the Italian Strong-Motion Network (IT) (Presidency Of Counsil Of Ministers-Civil Protection Department, 1972) and the Italian National Seismic Network (IV) (INGV Seismological Data Centre, 1997). The data that we used was downloaded from the Orfeus Engineering Strong-Motion database (ESM) (Luzi, Puglia, Russo, D'Amico, et al., 2016; Luzi, Puglia, Russo, & ORFEUS WG5, 2016).

Figure 1 shows the stations whose data were used in our inversion. Static displacements were recorded at all the 47 GNSS stations shown in the map, which are located within 60 km of the epicenter. Of these, 22 stations recorded high-rate GNSS displacements (black squares), whereas the remaining 25 stations only recorded the static field (blue squares). We used seismic data from the strong-motion stations closest to the epicenter (red circles). In particular, we selected data from 20 stations located at epicentral distances of less than 50 km, which allows for a direct comparison with previous studies that used the same data set (Gallovič et al., 2019b; Pizzi et al., 2017). The strong-motion data set consists of 20 three-component accelerograms, with the exception of station RQT, for which the N–S component was not available.

The static GNSS data used in our study were processed by three INGV data analysis centers; the detailed procedures can be found in Avallone et al. (2010) ; Cheloni et al. (2016); Serpelloni et al. (2012). In this work, we adopted the corrected data from Cheloni et al. (2017). The high-rate GNSS data is taken from Avallone et al. (2016), who processed the raw GNSS time-series using two different methods: Precise Point Positioning (PPP) (Bertiger et al., 2010; Zumberge et al., 1997) and Double-Difference (DD) (Herring et al., 2010), as implemented in the scientific packages GAMIT/GLOBK (http://geoweb.mit.edu/gg/) and Gipsy/Oasis (https://gipsy-oasis.jpl.nasa.gov/), respectively. The comparison between the results obtained by two methods shows a good agreement between the two sets of solutions. In this study, we use the high-rate GNSS time-series that result from the data processed with GIPSY/Oasis II. High-rate GNSS data were low-pass filtered with a corner frequency of 0.5 Hz.

After downloading the strong-motion accelerograms from ESM, we selected waveforms with a length of 32 s starting at the earthquake origin time. This time window includes the P- and S-waves at all stations. We applied a 0.05-taper Hanning window to strong-motion records in order to avoid cut-off effects at the edges of the waveforms. We then filtered the data with a band-pass fourth-order Butterworth filter between 0.05 and 0.5 Hz, which includes the 0.06–0.5 Hz band used in the inversion. Finally, we integrated the accelerograms into velocity waveforms. Both strong-motion and high-rate GNSS data were decimated to 4 sps ($\Delta t = 0.25$ sec) in order to speed up computations. We did not weigh the data explicitly, therefore all data point have an equal weight in the inversion.

Our data set is redundant in the high-frequency range ($0.06 < f < 0.5$ Hz), where both strong-motion and high-rate GNSS stations recorded the dynamic wavefield. We take advantage of this redundancy in order to assess the robustness of our model: We use the strong-motion accelerograms to constrain the slip model in this frequency range, and then use the inferred slip model to predict high-rate GNSS waveforms. The match between the amplitudes and phases of synthetic and observed GNSS waveforms not used in the inversion provides a measure of the adequacy of the slip model.

The velocity structure of the Central Apennines has been well studied by previous works focusing on the nearby 2009 L'Aquila M_w 6.3 earthquake. Here, we adopted the layered (one-dimensional) velocity-density-attenuation structure inferred by Ameri et al. (2012) (Table 1).

4. Parameterization of the Inversion

The adaptive approximation used in the neuro-fuzzy kinematic finite-fault inversion describes the spatial slip distribution at a given frequency using an arbitrary number of basis functions. The number of basis functions is established at the beginning of learning and remains constant throughout the learning process. If we use a small number of basis functions, then the number of parameters to be found is reduced. Accordingly, the size of the model-space and of the null-space is reduced as well. In order to have a formally over-determined problem, we should scale the number of model parameters so that they are less than the number of observed data points. Note that this requirement does not guarantee that the problem is well-posed, as observations are often not independent, which results in a rank-deficient, ill-conditioned problem. Rather, this formal over-determination is a simple rule of thumb to choose the number of fuzzy basis functions. Rank-deficiency is addressed by damping in the Tikhonov regularization (Hansen, 2005). In Section 6 we discuss an improved strategy to find a more adequate number of fuzzy basis functions for each data set based on a maximum likelihood approach.

In our application, we have 141 observations at 0 Hz, 66 observations between 0.03 and 0.06 Hz, and 59 observations at frequencies higher than 0.06 Hz. At each linear step of our hybrid inversion, the number of parameters to be found is given by the number of fuzzy basis functions along-strike (N_ξ) times the number of basis functions along dip (N_η). We need to consider two such systems, in order to account for slip in the along-strike (u_s) and updip (u_d) directions. Thus, at each inversion step, we will have a total of $2 \times N_\xi \times N_\eta$ model parameters. If we select $N_\xi = 6$ and $N_\eta = 4$, we will then have a total of $2 \times N_\xi \times N_\eta = 48$ model parameters to find at each frequency, which is less than the 59 minimum number of observation points. Therefore, we have an over-determined problem.

The fault location and geometry was set according to Gallovič et al. (2019b). In particular, we considered that the fault has a strike of 155° and a dip of 45°. As explained in the companion article, we use two different meshes: The integration mesh, which we use to evaluate the forward integral (Equation 8), and the regularization mesh, which we use to evaluate the smoothness condition (Equation 10). The forward mesh has dimensions of 2 km × 2 km and we considered either 4 or 9 Gaussian points within each integration sub-fault, depending on frequency. Table 2 summarizes the parameterization of the fault geometry and inversion parameters.

As described in the companion article, the regularizing parameter α is determined using an L-curve maximum curvature criterion (Kheirdast et al., 2021). L-curves plot the smoothness of the model, as measured by the squared Laplacian of the slip model, versus data misfit, as measured by an L2 norm. The point where L-curves have a maximum curvature corresponds to the smoothest model that can be found without deteriorating data fit significantly. Figure S2 shows the L-curves obtained at frequencies in the model range (0.00–0.5 Hz). As was the case for the synthetic test presented in the companion article, also here the maximum curvature point is easily distinguished at low frequencies ($f \leq 0.25$ Hz). However, at high frequencies ($f > 0.25$ Hz) the curvature of the L-curves decreases significantly and the adequate damping parameter becomes difficult to determine. This suggests that a more robust inversion at high frequencies would require the wavefield to be more adequately constrained, either by use of a higher resolution density-velocity model or by using a denser observational data set. In our method, it is possible to increase the accuracy of the forward modeling by increasing the number of Gaussian integration points (N_{gauss}). It is also possible to better tune the degree of smoothness by increasing the density of regularization points, which is achieved by reducing the spacing of the regularization mesh (Δx_r). Figure S2 shows that when we use finer grids, the maximum curvature of the L-curves becomes better defined, which is particularly important at high-frequencies ($f > 0.25$ Hz). Because finer grids increase the computational load, they are only advantageous at high frequencies. Accordingly, at low frequencies ($f \leq 0.25$ Hz) we use 4 Gaussian points inside each integration element and a distance between regularization points of 1 km. At frequencies above 0.25 Hz, we increase the number of Gaussian points inside integration elements from 4 to 9 and we reduce the distance between regularization points from 1 to 0.3 km.

If the damping parameter α cannot be found from the curvature of L-curves, nor from an assessment of data error, one can then follow a conservative approach and set the damping factor as close as possible to

Table 2
Parameterization of the Fault Geometry and Inversion

Hypocenter latitude	42.704 N
Hypocenter longitude	13.251 E
Origin-time	2016-08-24 01:36:32.702
Fault strike	155°
Fault dip	45°
Fault length	30 km
Fault width	14 km
Depth of the fault top edge	0.00 km
Depth of the fault bottom edge	9.89 km
Dimensions of the integration mesh	2×2 km
Number of Gaussian points (0–0.219 Hz)	2×2
Number of Gaussian points (0.25–0.5 Hz)	3×3
Dimensions of the regularization mesh (0–0.219 Hz)	1×1 km
Dimensions of the regularization mesh (0.25–0.5 Hz)	0.3×0.3 km
Waveform sampling period (dt)	0.25 s
Spectral sampling interval (df)	0.03 Hz
Number of Learning Epochs	200
Learning rate (κ)	0.01
Basis functions initialization method	Grid partitioning (Text S1)
Number of fuzzy basis functions along the strike direction (N_ξ)	6
Number of fuzzy basis functions along the dip direction (N_η)	4

Source parameters of the 2016 Amatrice Earthquake after Chiaraluce et al. (2017).

the large singular values in the inversion. This procedure may however over-damp the solution, that is, the solution will become stable at the cost of not using all the available information in the inversion.

5. Results

Figure 2 shows the slip solution obtained by applying our method to data of the Amatrice earthquake. The resulting frequency-dependent spatial slip distributions are plotted for both along-strike and updip components for chosen frequencies. As expected for a normal earthquake, the dip component displays higher amplitudes than the along-strike component. A region of slip to the NW of the hypocenter is consistently imaged at most frequencies. Note that our inversion is carried out independently for each frequency. The amplitude of the slip-rate spectrum decreases with increasing frequency, as expected given that the finite-duration of the source function acts as a low-pass filter (Bernard et al., 1996; Gallovič & Brokešová, 2004; Gallovič, 2006). The fact that the main region of slip is consistently imaged at various frequencies indicates a stable solution.

We can easily transform the complex-valued frequency domain source function to time-domain slip-rate functions by Fourier analysis. We start by selecting representative points on the fault (ξ_0, η_0) and creating source time functions spectra at those points from the fuzzy approximation (Equations 2 and 3). We then obtain time-domain source functions from the spectral source functions by inverse Fourier transform. Figure 3 shows the resulting source function obtained from the fuzzy approximation method in the spatio-temporal domain. In the background of Figure 3a, we presented the static (0 Hz) dislocation, which
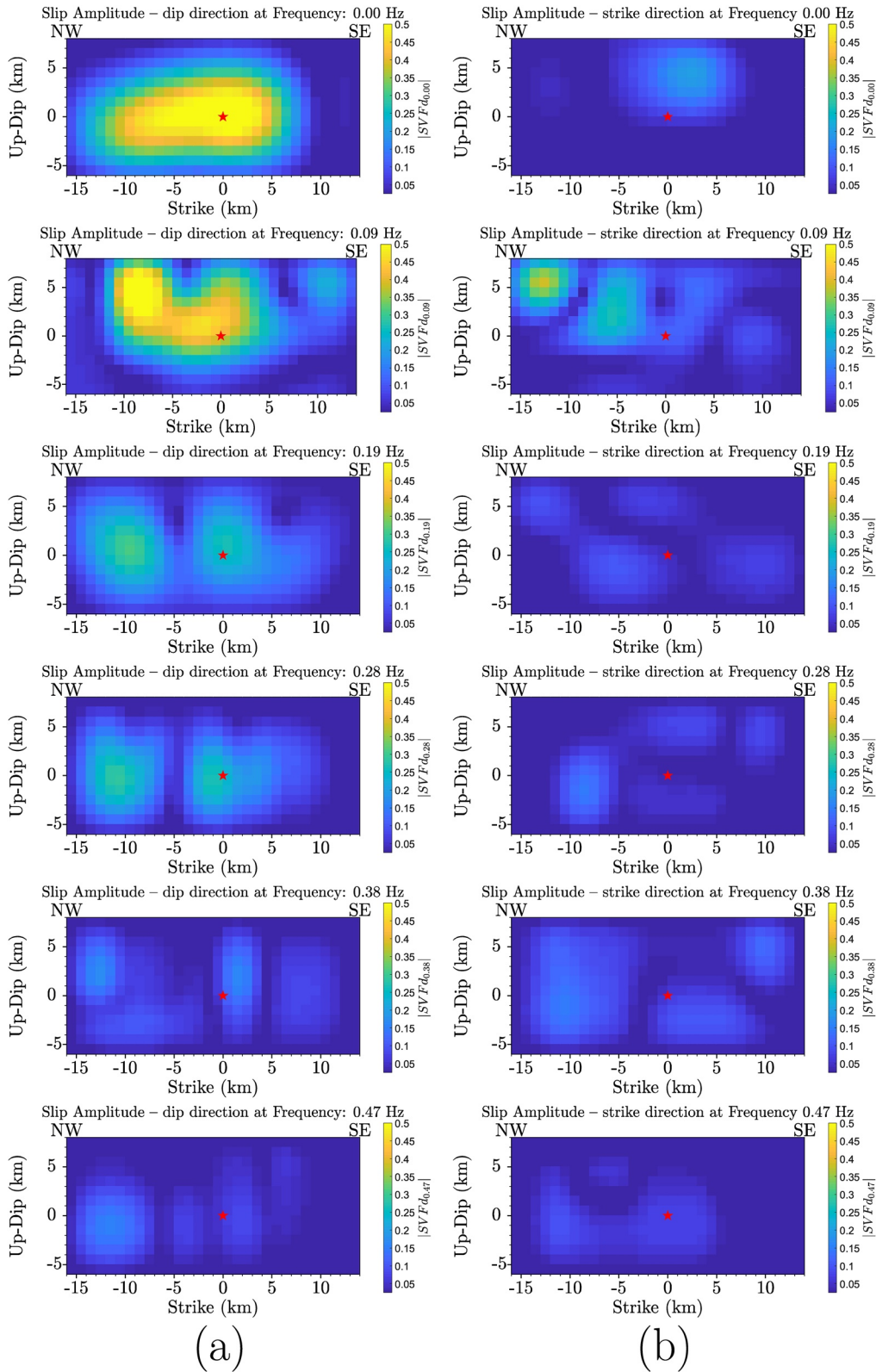
Figure 2. Spectral amplitudes of the inverted source function in both (a) updip and (b) along-strike directions, at selected frequencies. Spectral source functions have higher amplitudes in the updip direction than along strike, indicating that faulting is mostly normal. Rupture asperities at different frequencies are located approximately within the same regions, which indicates a good quality solution. The full version of the figure, showing slip spectral amplitudes at all frequencies, is provided in the electronic supplement (Figure S3).
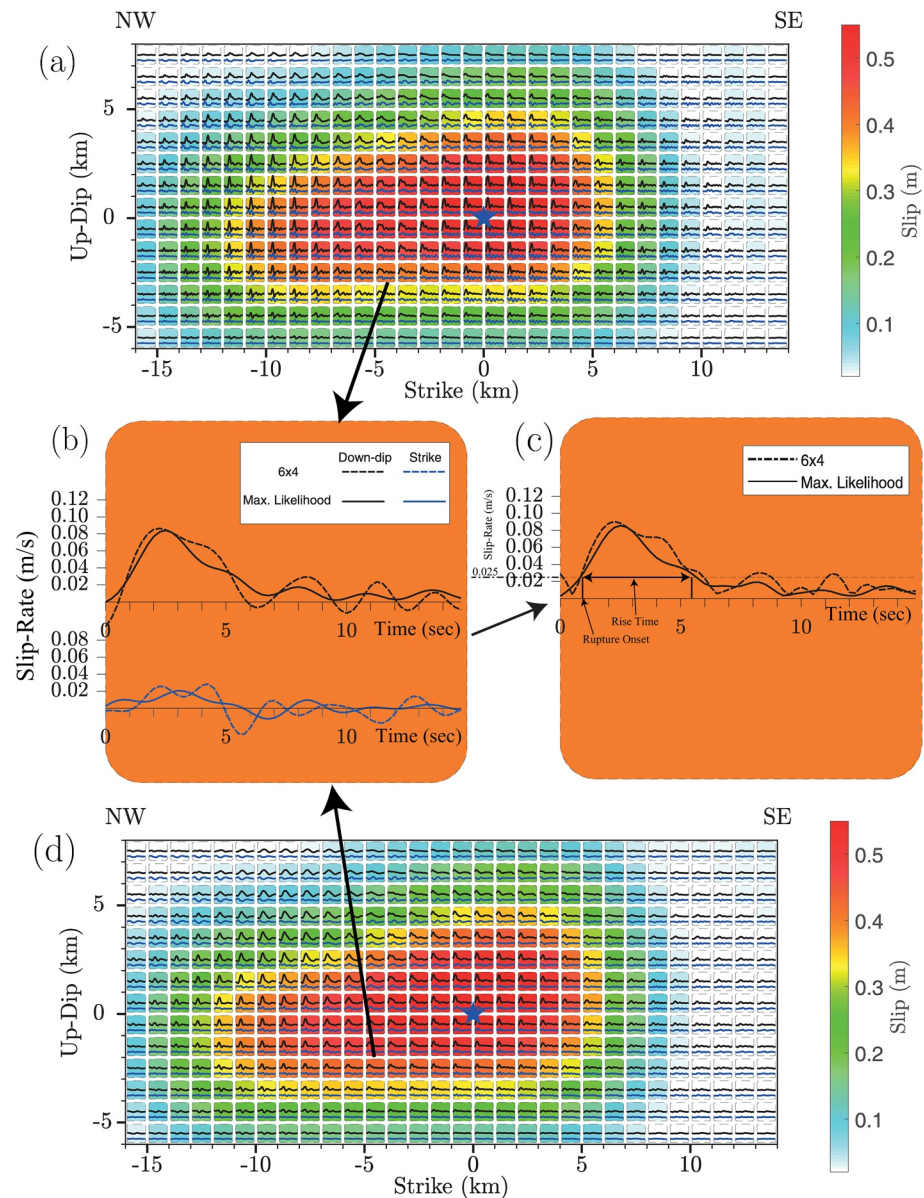
Figure 3. Kinematic source function obtained by the neuro-fuzzy inversion method for the Amatrice earthquake, shown in representative 1×1 km^2 cells. (a) The number of basis functions was selected using the rule of thumb presented in Section 4, which simply ensures that the inverse problem is over-determined. The colored background shows the static (0 Hz) dislocation, which corresponds to the cumulative slip on the fault, as inferred from static GNSS data. Individual cells display the time-domain slip rates in both down-dip (black) and along-strike (blue) components. The blue star marks the hypocenter determined by Chiaraluce et al. (2017). (b) Enlarged image of one of the points on the fault using both the maximum likelihood (full line) and over-determined (dashed line) solutions. Note that because the faulting mechanism is normal, the dip component of the dislocation vector points toward the down-dip, and the dip component of slip-rate (black-line) is plotted positive down-dip. (c) Total amplitude of the slip velocity as given by the vectorial sum of the down-dip and along strike components, $\sqrt{u_s(\xi,\eta,t)^2 + u_d(\xi,\eta,t)^2}$. (d) Inverted slip function obtained from the maximum likelihood method. The final slip is shown in the background, the slip-rate function at representative points is plotted inside the squares for both down-dip (black) and strike (blue) directions.

corresponds to the cumulative slip on the fault, as inferred from the static GNSS data (colored square cells). Each cell in Figure 3a shows the time-domain slip rates in both down-dip (black) and along-strike (blue) components. Figure 3b shows a zoom of the source time function for one of the points on the fault, plotted with the dashed line. Because the faulting mechanism is normal, the dislocation vector points toward
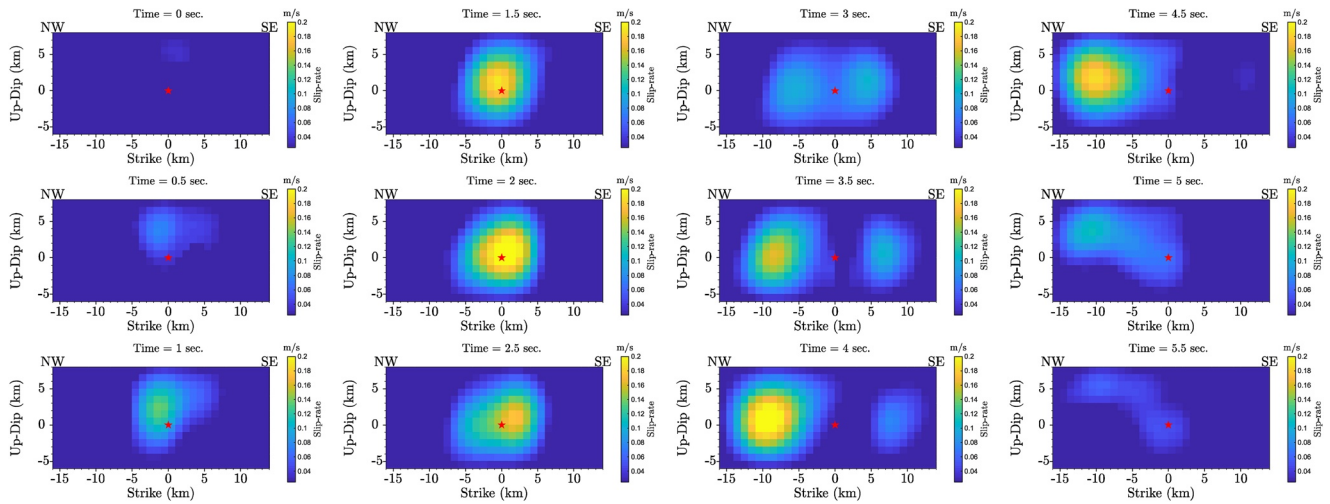
Figure 4. Slip-rate amplitudes at 0.5 s time steps. The rupture nucleates at shallow depths and then propagates bilaterally. The red star marks the hypocenter determined by Chiaraluce et al. (2017). The slip-rate functions at each point on the fault plane are plotted in Figure 3a. An animated version of this figure is provided in the electronic supplement.

down-dip and the slip-rate diagram in Figure 3b is positive in the down-dip direction. In order to suppress the cut-off frequency effect in the inverse Fourier transform, we tapered the spectrum using a cosine filter. Slip-rates show some undesired ripples, including minor backslip. We discuss these fluctuations in Section 7.2; We will see in the next section that it is possible to mitigate this effect by increasing the accuracy of modeling.

Figure 4 shows the amplitude of the slip velocity at consecutive time steps, displaying snapshots of the rupture process. The amplitude of the slip velocity is given by the vectorial sum of the updip and along strike components, that is, by $\sqrt{u_s(\xi, \eta, t)^2 + u_d(\xi, \eta, t)^2}$. In order to highlight the rupture areas, we do not show slip rates below 0.025 m/s (ref. Figure 3c). In our model the rupture nucleates at shallow levels and grows slowly for two seconds. The rupture then starts to spread bilaterally, both toward the NW and SE, with higher slip rates toward the NW. The characteristics of the inferred rupture are discussed in detail in Section 7.1. The synthetic ground-motion waveforms simulated using the source functions obtained in this section are compared with the observed strong-motion data in the supplemental material. Figure S4 shows the time-domain comparison between the strong-motion records and synthetic ground-motions. The synthetic waveforms are ordered based on their distance from the hypocenter. It is worth noting that the directivity pulse is perfectly reconstructed at station AMT (Figure S4). Although the arrival phases and the amplitudes are well approximated in the synthetics, at some far stations (e.g., ASP, SPM, and TRE) the synthetic waveforms do not reconstruct the observed data properly. Figure S5 (red-line) shows the spectral comparison between observed and synthetic ground motion. The comparison between observed and synthetic static (0 Hz) displacement is shown in Figure S6. In the next section, we present a maximum likelihood approach to select an adequate number of fuzzy basis functions, which is better able to recover model information from the observed data.

6. A Maximum-Likelihood Approach to Select an Adequate Number of Fuzzy Basis Functions.

In the companion article, we showed that the neuro-fuzzy inversion method allows to use few basis functions to spatially discretize the slip function at each frequency, thus reducing the number of small singular values and stabilizing the inverse problem. Accordingly, it is advantageous to discretize the fault plane using the smallest number of basis functions that still allows to resolve the rupture process. In the previous section, we solved the inversion using 6 × 4 fuzzy basis functions, which yielded a formally over-determined

problem. In alternative, we can use a better informed maximum likelihood approach to select a more appropriate number of basis functions.

In order to gain a deeper understanding on the impact of varying the number of fuzzy basis functions, let us start by considering various sets of fuzzy basis functions. In particular, Figure 5 shows the results of inversions using 84 different configurations of fuzzy basis functions, varying between 4×4 and 15×10 fuzzy basis functions. The number of integration points, as well as the distance between the regularizing points, are the same as shown in Table 2. Figure 5a shows the L-curves for the various inversions, at the first learning epoch, for selected frequencies. Red circles mark the maximum curvature points. The variable number of fuzzy basis functions impacts significantly the choice of the damping factor α, which in turn determines the acceptable level of misfit, that is, how well the model will aim to fit the data.

The residual norm, or misfit, $\left\| \mathbf{GWA} - \mathbf{d} \right\|_2$, at the maximum curvature point may be interpreted as a rough estimation of the amount of uncertainty or noise in the inversion, and corresponds to the misfit level tolerated (Hansen, 2005, p. 84). Figure 5b shows a histogram of the residual norms inferred from the various inversions, or equivalently, of the uncertainty level tolerated, as inferred from the various inversions carried out with different sets of fuzzy basis functions. We take as the most likely uncertainty value that which is given by the maximum-likelihood misfit bin. Figure 5c plots the estimated amount of uncertainty in the inversion versus the total number of fuzzy basis functions. The adequate discretization is chosen as that with a lowest number of model parameters among those with the most likely uncertainty. Table 3 lists the maximum-likelihood sets of fuzzy basis functions inferred for each frequency. In general, the adequate number of fuzzy basis functions increases with increasing frequency, as would be expected given that more spatial detail is needed to resolve shorter wavelengths. Figure 5b also shows the dispersion of the uncertainty estimates obtained from the maximum curvature criterion. The histograms at low frequencies indicate that at low frequencies one can equally use many or only a few fuzzy basis functions without affecting data fit. However, at high frequencies more fuzzy basis functions are needed in order to obtain a model with enough detail to fit the data.

Figure 6 compares the spatial distribution of updip slip amplitude obtained using: (a) 6×4 fuzzy basis functions, according to the simple over-determination criterion presented in Section 4; (b) a variable number of fuzzy basis functions at each frequency, according to the maximum likelihood approach discussed in this section. At low frequencies, the results of the two methods are very similar. However, at high frequencies (>0.25 Hz), the maximum likelihood approach is able to provide a more detailed picture of the rupture process, because it uses a higher number of fuzzy basis functions. In turn, the increased detail of the rupture process at high frequencies ensures an improved data fit. The full inferred amplitudes of the spatial slip distributions for both along-strike and updip components using the maximum-likelihood method are provided in the supplemental material (Figure S8).

Figure 3d shows the source time functions obtained using the maximum likelihood approach. The comparison between Figures 3a and 3d shows that identical static slip distributions are obtained in the two cases. However, the slip rates obtained from the maximum likelihood approach (Figures 3b, and 3c-full line) show less ripples and also less back slip, which indicates a better constrained high-frequency inversion. Figure 8 compares the observed velocity waveforms (black) at the strong-motion stations (Figure 1) and the synthetic traces (red) obtained from the maximum likelihood method. Both traces are band-pass filtered in the strong-motion frequency range 0.06–0.5 Hz. Figure S5 (blue-line) shows the the corresponding spectral comparison between the observed and synthetic ground motion. Figure 7 shows the comparison between the observed and synthetic static displacement. The comparison between synthetic waveforms obtained from the over-determined approach (6×4) (Figure S4) and those from the maximum likelihood approach (Figure 8) shows that the latter can better approximate the observed amplitudes and arrival phases. In addition, synthetic waveforms can better simulate the ground-motion at far stations.

Figure S10 shows the evolution of the basis functions, with the basis functions plotted at the start and end of the learning process. It is worth noting that both the center (μ) and spread (σ) of the basis functions evolve during the inversion, as to enhance both data fit and model smoothness.
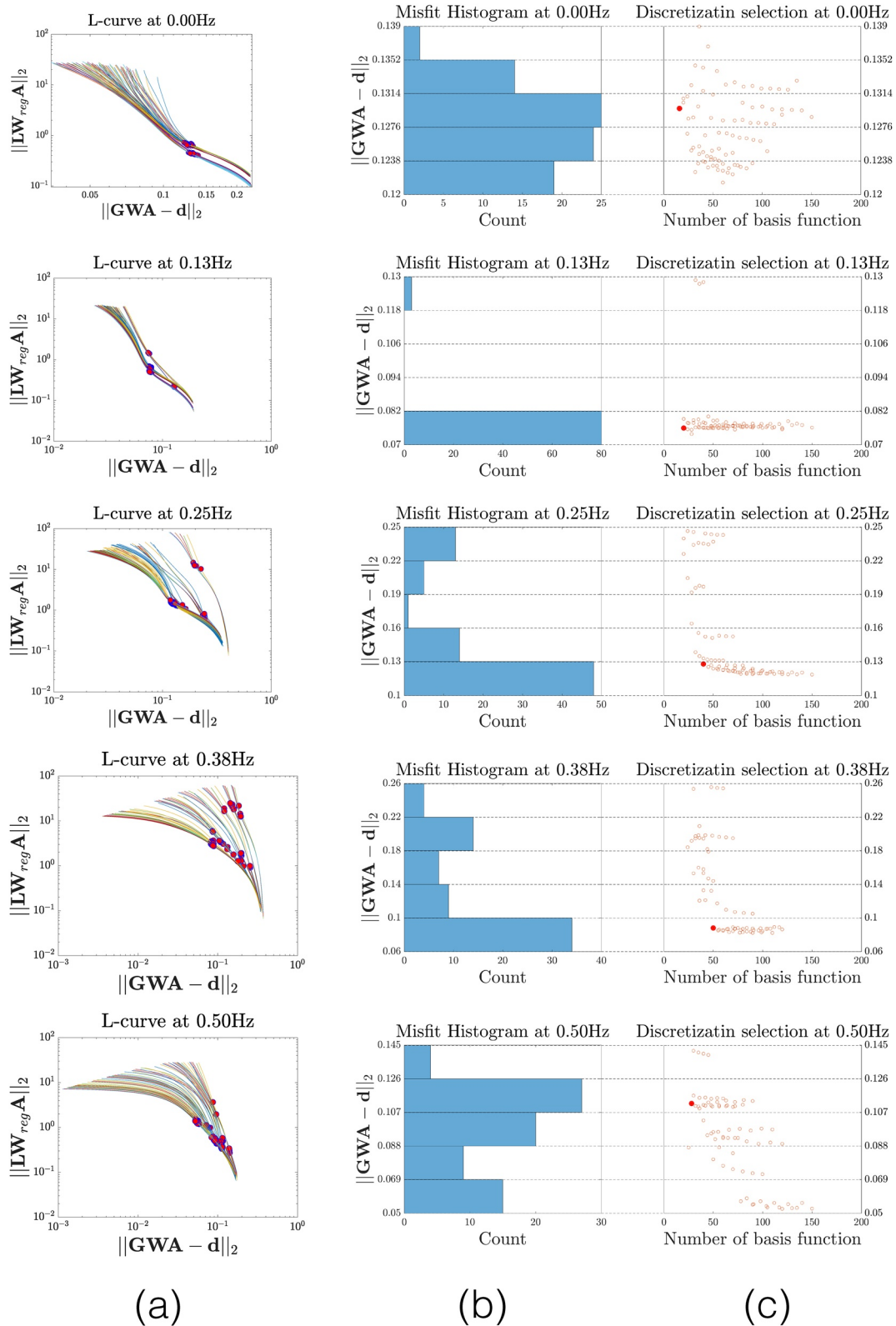
Figure 5

Table 3
Selected Number of Fuzzy Basis Functions at the Various Model Frequencies

Frequency (Hz)	Selected Number of fuzzy basis functions Total: $(N_\xi \times N_\eta)$	Maximum Likelihood: Residual norm [m/s] First epoch (Figure 5c)	Final epoch	Over-determined (6×4) Final residual norm [m/s]	Validation data (GNSS): Residual norm [m/s] Maximum likelihood	Over-determined (6×4)
0.000	16 (4 × 4)	0.12972	0.11790	0.11850	-	-
0.031	32 (8 × 4)	0.08808	0.08684	0.08770	-	-
0.063	16 (4 × 4)	0.10899	0.10264	0.09850	-	-
0.094	24 (6 × 4)	0.05105	0.04545	0.04545	0.13676	0.13676
0.125	20 (4 × 5)	0.07601	0.06532	0.07222	0.15811	0.15797
0.156	16 (4 × 4)	0.08469	0.07271	0.07847	0.21847	0.21914
0.188	72 (12 × 6)	0.09186	0.08342	0.10305	0.26043	0.26111
0.219	28 (7 × 4)	0.11591	0.10274	0.14911	0.31821	0.31695
0.250	40 (8 × 5)	0.12804	0.11498	0.18384	0.36243	0.35401
0.281	40 (10 × 4)	0.15869	0.14580	0.20557	0.39028	0.35584
0.313	40 (10 × 4)	0.13836	0.12375	0.21674	0.47089	0.46310
0.344	50 (10 × 5)	0.10598	0.09014	0.22757	0.48202	0.49457
0.375	50 (10 × 5)	0.08824	0.07016	0.22687	0.55692	0.50920
0.406	50 (10 × 5)	0.11507	0.09067	0.20738	0.44197	0.43898
0.438	44 (11 × 4)	0.15204	0.13177	0.20006	0.59006	0.62687
0.469	32 (8 × 4)	0.14264	0.12366	0.14419	0.50622	0.51261
0.500	28 (7 × 4)	0.11214	0.09235	0.10875	0.39344	0.39506

Note. At higher frequencies, more fuzzy basis functions are needed in order to lower the misfit to its maximum-likelihood value. The double lines separate inversions based on different datasets (static GNSS, HR-GNSS and strong-motion). The residual norm, $\left\| \mathbf{GWA} - \mathbf{d} \right\|_2$ is shown at the beginning and the end of the learning process. when the number of discretizations is selected using the maximum likelihood (Section 6), the residual norm at almost all frequencies, is less than when using the over-determined rule of thumb. the residual norms obtained from the maximum likelihood and over-determined procedures for the validation data set (high-rate GNSS) are similar.

Figure 5. Maximum likelihood approach used to select an adequate number of fuzzy basis function. (a) L-curves obtained using 84 different configurations of fuzzy basis functions, varying between 4 × 4 and 15 × 10. Red circles mark the maximum curvature points. We assume that the misfit value (abscissa) at the maximum curvature point provides a good estimate of the value of uncertainty (noise) in each inversion. (b) Histogram of misfit values at the maximum curvature point, considering all inversions using various sets of fuzzy basis functions. The most likely bin corresponds to the most likely uncertainty (noise) level. (c) Circles indicating the amount of uncertainty inferred from the inversions using different numbers of fuzzy basis functions. Horizontal dashed lines correspond to the boundaries of the histogram bins. The red circle marks the adequate discretization, which corresponds to the minimum number of fuzzy basis functions in the maximum-likelihood misfit bin. A similar figure but for the full range of solution frequencies is provided in the supplemental material (Figure S7).
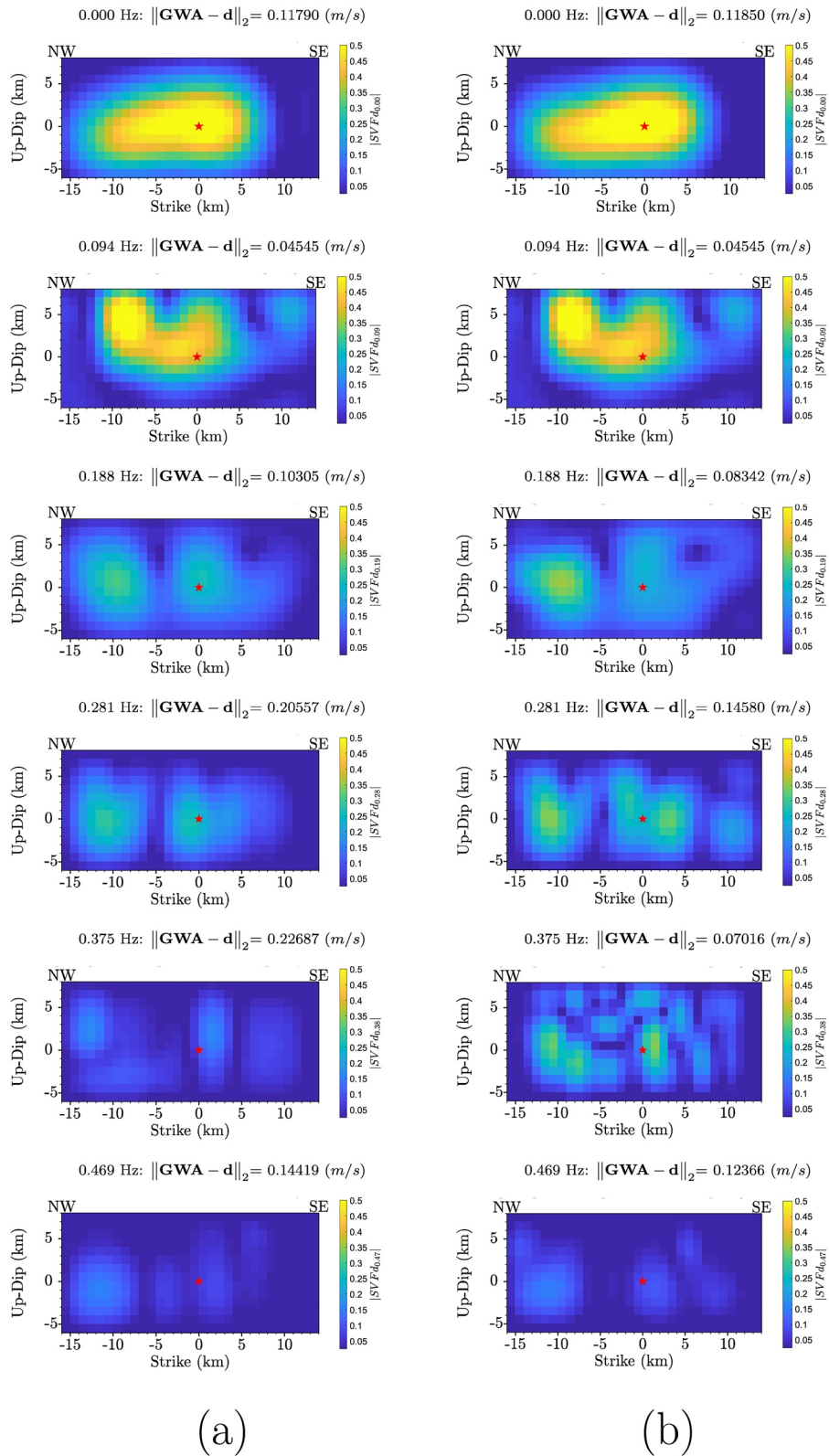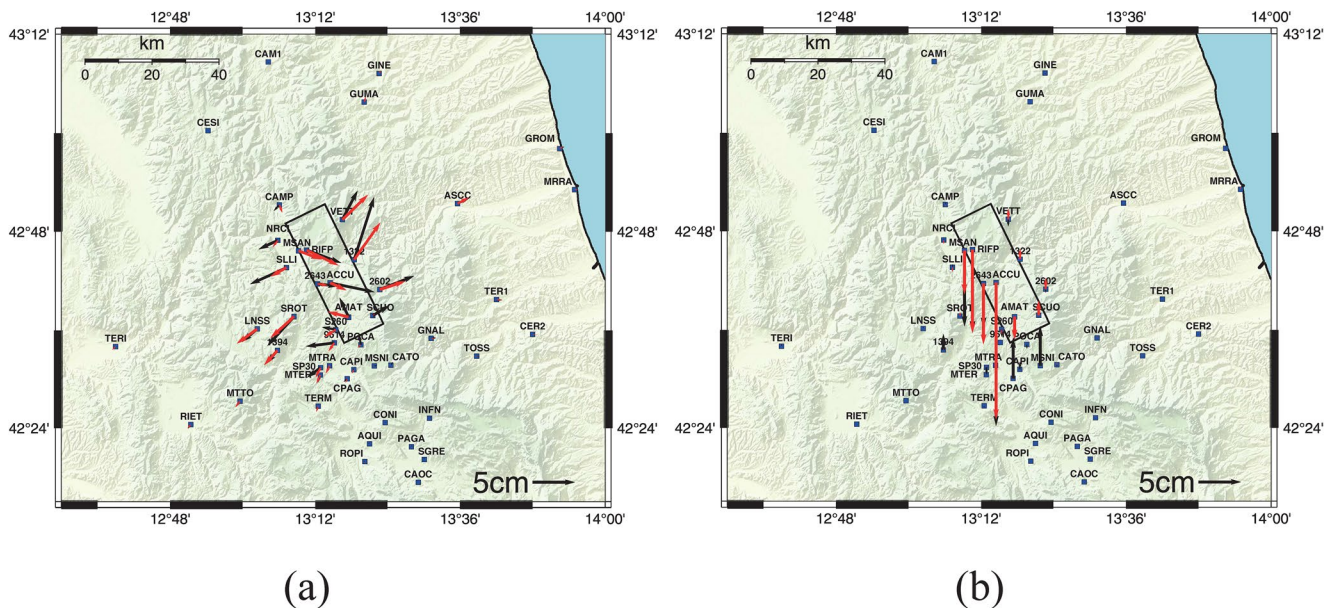
Figure 6

(a) (b)

Figure 7. Comparison between observed static surface displacements (black arrows) and synthetics (red arrows), in both: (a) Horizontal direction (NS and EW), and (b) Vertical direction (positive upwards). Synthetics are obtained from the inversion based on the maximum likelihood approach for fault discretization presented in Section 6.

7. Discussion

In this section, we discuss the performance of the neuro-fuzzy inversion method. In particular, we compare our rupture model with those inferred from previous studies (Section 7.1), we discuss back slip in our model (Section 7.2), we discuss the strategies presented in this article to find an adequate number of fuzzy basis functions (Section 7.3), and finally we validate our model by predicting ground motion at sites whose data was not used in the inversion (Section 7.4).

Note that our solution is shown only up to 0.5 Hz. In general, most finite-fault inversions are limited to low-frequencies (Ide, 2015). Two main arguments explain the limitations of kinematic finite-fault inversions in modeling high-frequency ground motion. One limitation is the accuracy of the velocity-density-attenuation model, as well as the ability to forward model the complexities of the wavefield at high frequencies, including effects such as topography, site effects, etc., When our knowledge of the crustal structure is insufficient to model the wavefield at short wavelengths (high frequencies), or when the simulation method (for example, the DWN method Bouchon, 2003) does not allow for the consideration of Earth complexities, then the inversion is also unable to resolve the source function at high frequencies. From this viewpoint, the high frequency limit is usually determined by considering the minimum wavelength that can reliably be modeled given the available information on the crustal structure (e.g., Somala et al., 2018). For example, Sokos and Zahradník (2013) suggests that considering the existing crustal models, one can usually invert near stations (<~1km) up to <~1 Hz, whereas near-regional stations (~100 km) can be inverted up to ~0.1 Hz, and regional stations ~1000 km up to ~0.01 Hz. In the case of Amatrice earthquake, Tinti et al. (2016) used the maximum frequency of 0.5 Hz to avoid unknown local uncertainties, such as site effects. The same upper limit was used by Cirella et al. (2018), who adopted the IMAGINE-IT model (Casarotti et al., 2016). A similar upper bound limit was adopted by Pizzi et al. (2017) and Gallovič et al. (2019b).

Figure 6. Comparison between updip slip at selected frequencies. (a) Slip model obtained using 6×4 fuzzy basis functions, according to the simple over-determination criterion presented in Section 4. (b) Slip model obtained using a variable number of fuzzy basis functions at each frequency, determined using the better informed maximum likelihood approach discussed in Section 6. The slip models obtained from two inversions display similar patterns at low frequencies. However, at higher frequencies the maximum likelihood approach reveals more detail, as it uses a higher number of basis functions, which are needed to adequately describe the observations at high frequencies. The full range of solutions obtained for all frequency points is provided in the supplemental material (Figure S9).
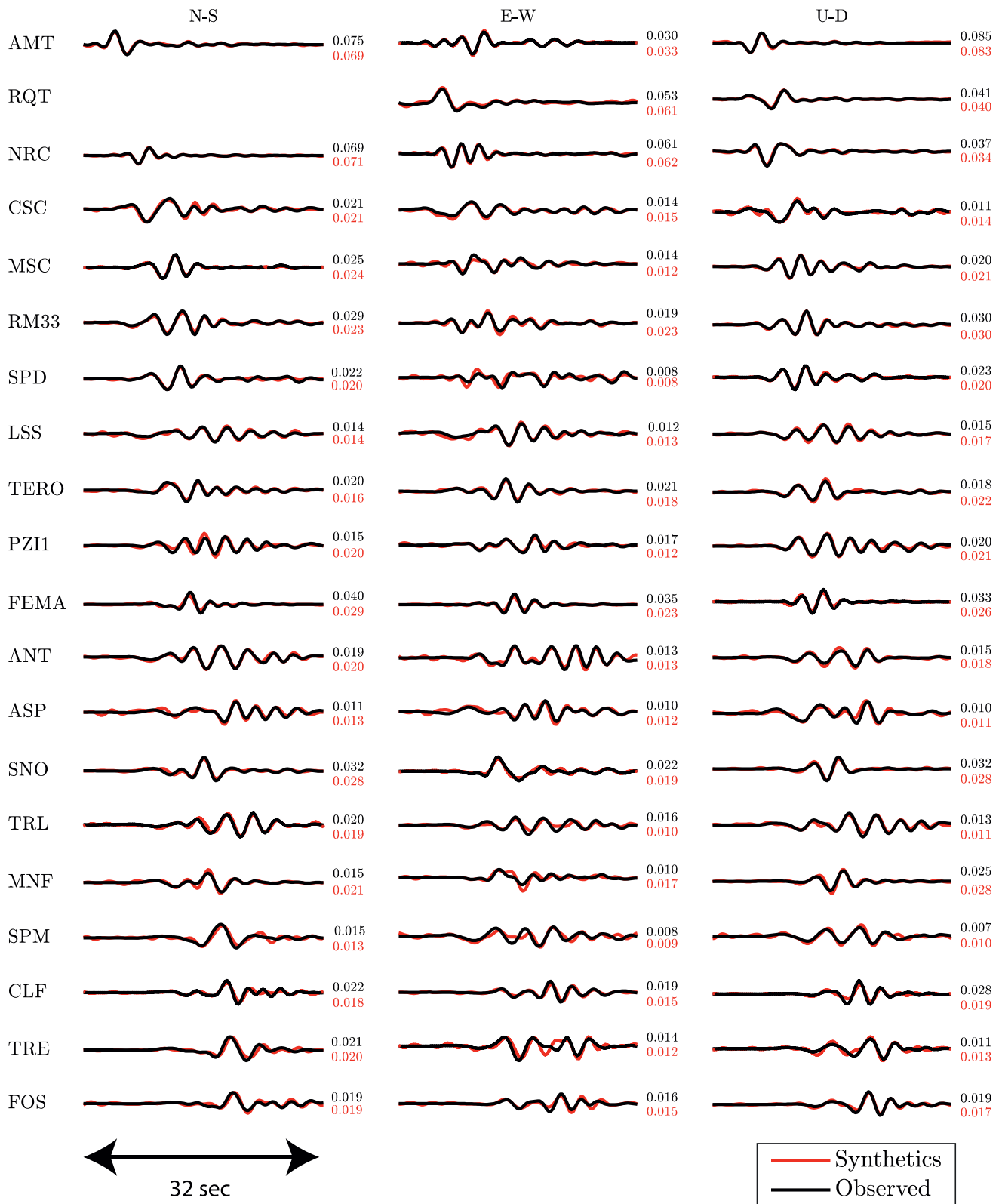
Figure 8. Comparison between synthetics and observed velocities at strong-motion stations. Observed waveforms are plotted in black and synthetic traces found using the maximum likelihood approach (Section 6) are plotted in red. The maximum trace amplitudes (m/s) are shown in front of each station component. Waveforms are band-pass filtered in the frequency range 0.06–0.5 Hz, where we used the strong-motion data to infer the source function.

A second argument arises from the ill-posed nature of the inverse problem. Let us consider the generalized singular value decomposition (GSVD) analysis presented in the companion article (Kheirdast et al., 2021). Consider the cost associated with the roughness of the model, $Cost_{smooth}$, and the solution residual norm $Cost_{data}$, which can be expanded as Equation 27 and Equation 30 (Supporting Information S4 in Kheirdast et al., 2021). The $Cost_{data}$ is expanded based on images of data on data basis ($\mathbf{U}_{:,i}^{\mathbf{T}}\mathbf{d}_{\omega_j}$), while $Cost_{smooth}$ is expanded by $\frac{\mathbf{U}_{:,i}^{\mathbf{T}}\mathbf{d}_{\omega_j}}{\gamma_i}$. Figure S11 shows how ($\mathbf{U}_{:,i}^{\mathbf{T}}\mathbf{d}_{\omega_j}$) and $\frac{\mathbf{U}_{:,i}^{\mathbf{T}}\mathbf{d}_{\omega_j}}{\gamma_i}$ are arranged in the range of generalised singular values (γ_i). Note that large values of $\mathbf{U}_{:,i}^{\mathbf{T}}\mathbf{d}_{\omega_j}$ helps us to gain information from the data while large values of $\frac{\mathbf{U}_{:,i}^{\mathbf{T}}\mathbf{d}_{\omega_j}}{\gamma_i}$ render the problem unstable. When the large values of $\mathbf{U}_{:,i}^{\mathbf{T}}\mathbf{d}_{\omega_j}$ can be separated from large values of $\frac{\mathbf{U}_{:,i}^{\mathbf{T}}\mathbf{d}_{\omega_j}}{\gamma_i}$, we can easily distinguish a proper cut-off α, and we can use the singular values that are needed to solve the inverse solution in a stable manner, without loosing too much information.

In Figure S11, this is the case for the inversion at a low frequency. When we move to a higher frequency, the image of data on data space basis ($\mathbf{U}_{:,i}^{\mathbf{T}}\mathbf{d}_{\omega_j}$) on the range of small singular values increases. Because we filter out small singular values by applying a regularizing constraint, we loose more information at high-frequencies in comparison with lower frequencies. Consequently, the value of $Cost_{data}$ increases with increasing frequency. A similar analysis on the behavior of ($\mathbf{U}^{\mathbf{T}}\mathbf{d}$), when components of frequencies higher than 0.2–0.3 Hz are inverted, was previously presented by Gallovič and Zahradník (2011) and Gallovič and Ampuero (2015) in time-domain inversions. The forward modeling based on the representation theorem is equivalent in time and frequency domains, therefore the accuracy of the forward model does not differ between frequency and time-domain formulations.

It should be noted that the foregoing arguments do not provide an exact high-frequency limit for kinematic inversions.

7.1. Comparison With Previous Studies

Previous studies characterized in detail the source kinematics of the Aug/24/2016 Amatrice earthquake (Aochi & Twardzik, 2019; Cirella et al., 2018; Gallovič et al., 2019b; Huang et al., 2017; Pizzi et al., 2017; Tinti et al., 2016). Most studies agree on the general features of the earthquake, namely on a weak nucleation phase, a bilateral rupture propagation, and a high-slip patch NW of the hypocenter. Here, we compare our rupture model in detail with those obtained by Aochi and Twardzik (2019); Gallovič et al. (2019b); Pizzi et al. (2017). The model by Pizzi et al. (2017) results from a kinematic inversion based on the method of Gallovič et al. (2015), which attained the top rank in the SIV benchmark exercise (Mai et al., 2016). The models by Aochi and Twardzik (2019); Gallovič et al. (2019b) result from dynamic modeling and takes into account the physics of rupture. In order to facilitate the comparison, several of our modeling assumptions, including the density-velocity model and the strong-motion data set, were chosen to be identical to those used by Gallovič et al. (2019b); Pizzi et al. (2017) (Section 4).

Most finite-fault inversions are carried out in the time-domain, therefore we need to reconstruct carefully the time-domain rupture parameters in order to allow the comparison. In particular, the neuro-fuzzy inversion method does not compute the rupture arrival time explicitly. Arrival time must then be obtained from the slip-rate functions. The rupture time corresponds to the time when a given point on the fault starts to slip. This may corresponds to an abrupt change in the slip-rate value, which marks the onset of slip. An exact estimation of the rupture arrival time thus requires a good reconstruction of the high-frequency components of the slip-rate function. We inferred the rupture time from our model as the time when the slip-rate at a given points exceeds a minimum value, which we set to 0.025 m/s (Figure 3c). Similarly, we considered that a given point on the fault heals (i.e., stops slipping) when the slip rate falls below the same threshold value of 0.025 m/s. The 0.025 m/s threshold was chosen as to prevent low-amplitude ripples to affect our results. This implies that in estimation of rupture and rise-time parameters, when the slip rate is
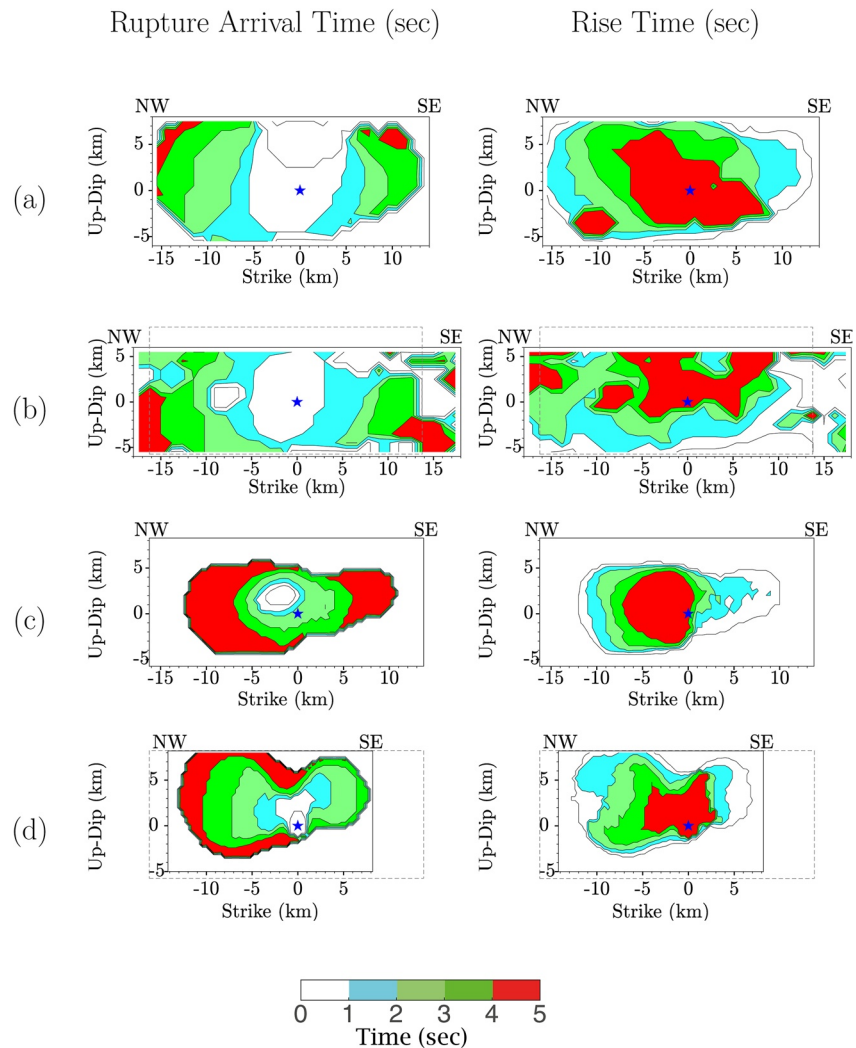
Rupture Arrival Time (sec)   Rise Time (sec)

Figure 9. Rupture arrival time (left) and rise time (right) of the Amatrice earthquake, as obtained by (a) this study; (b) Pizzi et al. (2017); (c) Gallovič et al. (2019b); and (d) Aochi and Twardzik (2019). The slip solution shown here is that obtained in Section 6, using a maximum likelihood approach to determine the adequate number of fuzzy basis functions. We considered the rupture arrival time as the first time when the slip rate raises above a threshold value of 0.025 m/s (Figure 3c). The rise time is defined as the time span during which the slip rate is above 0.025 m/s. The blue asterisk in (a, b, c) marks the hypocenter reported by Chiaraluce et al. (2017), and in (d) shows the hypocenter reported by INGV http://terremoti.ingv.it/en/event/7073641.

less than 0.025 m/s, we effectively consider it as zero. Additionally, we define the rise time as the sum of all time windows when the fault is slipping, that is, when the slip rate is above the threshold value of 0.025 m/s. Note that we do not impose time-domain constraints, therefore a given point on the fault is freely allowed to stop slipping and later re-start to slip. Note also that the rupture arrival times and rise times thus found are simple estimates, built to allow the comparison with previous studies, and not accurate reconstruction.

Figure 9 shows the arrival time and rise time estimated from our more robust solution, which is obtained by selecting an adequate number of fuzzy basis functions using the maximum likelihood approach (Figure 3c). For comparison, we also show the arrival and rise times of Aochi and Twardzik (2019); Gallovič et al. (2019b); Pizzi et al. (2017) calculated from their respective source time functions, using the same approach as we used for our solution. The source function of Pizzi et al. (2017) was accessed from SRCMOD database (Mai & Thingbaijam, 2014) and the solutions of Aochi and Twardzik (2019); Gallovič et al. (2019b) were obtained from the authors directly. Our solution confirms a bilateral rupture propagation, as proposed by previous works (Figure 9). Note that in our inversion slip is not constrained to start at a pre-determined
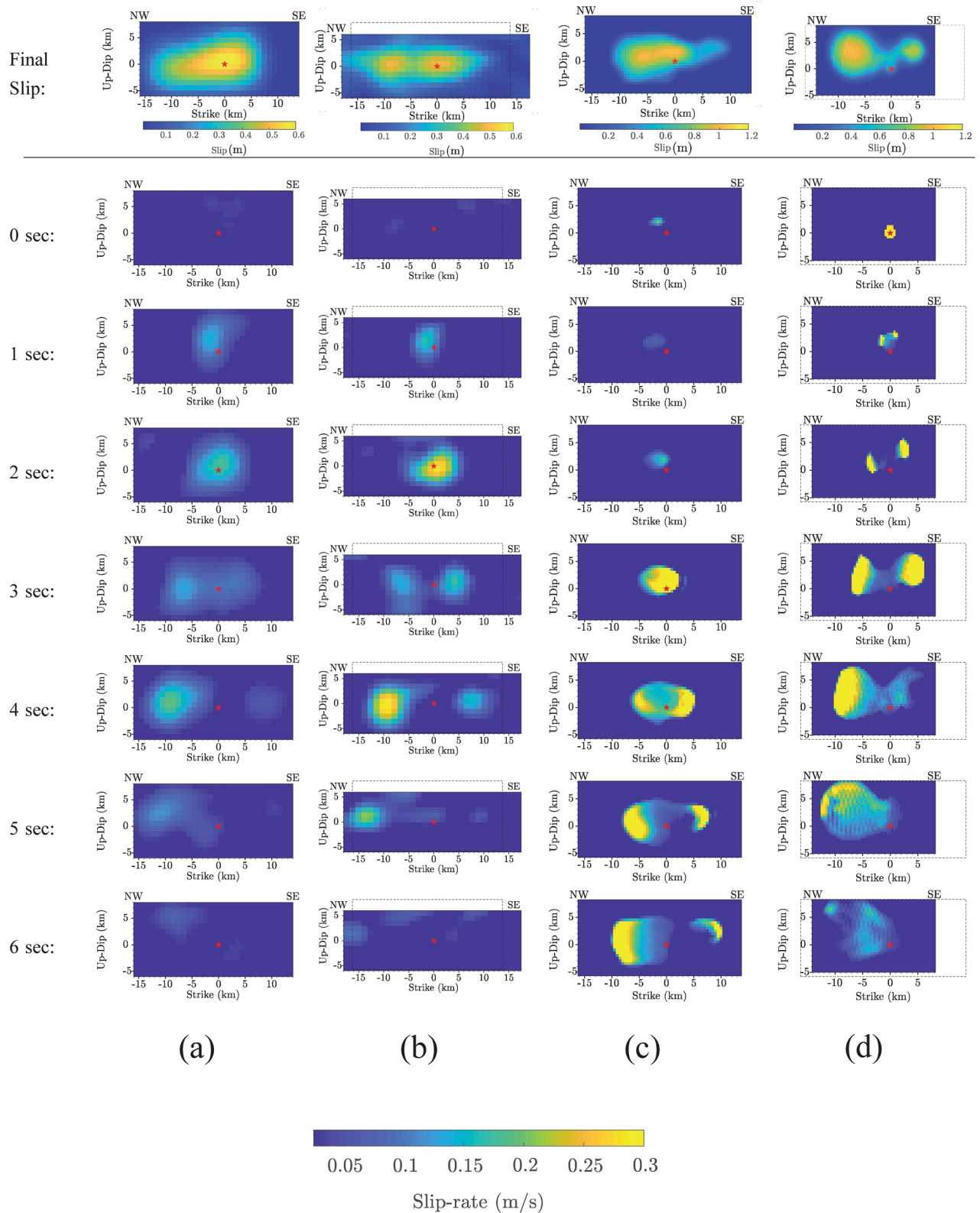
Figure 10

hypocenter. Figure 10a shows that in our maximum likelihood solution the earthquake nucleates at shallow depths, around ∼3.9 km, then moves down dip, pauses briefly, and then starts to spread bilaterally. However, in previous solutions such shallow nucleation and down dip propagating rupture is not apparent. We should emphasize that due to the low spatial resolution (Section 5.6 of Kheirdast et al., 2021), limited ability to invert high-frequency components of ground-motion, and epistemic uncertainties in modeling assumptions (Ragon et al., 2018), our method fails to infer small scale features of the slip function, such as hypocentral point.

The nucleation phase is relatively slow, reaching a maximum slip-rate 2 s after the origin time. In our solution, similar to the dynamic models of Aochi and Twardzik (2019); Gallovič et al. (2019b), the hypocentral region has a higher rise-time value (∼5 sec) than the rest of the fault, which indicates a slow process of stress release. This value then decreases gradually to both sides of the hypocenter until the rupture stops. However, the solution by Pizzi et al. (2017) shows a shallower area with a longer rise time (∼5 sec) than other solutions. In our solution, after ∼4 − 5 seconds, the rupture stops to the SE of the hypocenter. To the NW of the hypocenter, the fault continues to rupture until ∼6.5 seconds after the origin time. The ruptured area covers $25 \times 13 \text{km}^2$ of the assumed fault plane, an area that is, comparable with that inferred from the kinematic inversion of Pizzi et al. (2017) and larger than that found by the dynamic inversions. The cumulative slip distribution that we obtained is mostly concentrated to the NNW of the hypocenter, similar to what was previously observed by selected solutions (final slip row in Figure 10).

Figure 10 shows that our solution is geometrically and chronologically similar to that of Pizzi et al. (2017) (Figure 10b). However, the slip-rate amplitude in Pizzi et al. (2017) is higher than in ours. This may result from two main reasons: (a) Weights applied to the observed data: In our solution the data are not weighted, thus all observations contribute equally to the final solution. By weighting observations without considering their uncertainty, one will give more importance to observations that may be affected by larger errors, thus introducing noise in the model parameters. In our understanding, equal weighting more appropriately reflects our lack of knowledge on data uncertainty. (b) The strength of the regularization method: In our method, each solution frequency is subjected to one regularizing constraint, which can significantly dampen the inversion. Pizzi et al. (2017), on the other hand, applied a single regularizing constraint to the entire time-space model parameters, including spatio-temporal smoothness, seismic moment constraint, and no backslip (i.e., a given point on the fault must always slip in the same direction). The stronger regularization constraints in our model may result in lower amplitude slip-rates.

Figures 10c and 10d show slip-rate snapshots obtained from the dynamic inversions of Gallovič et al. (2019b) and Aochi and Twardzik (2019), respectively. Both dynamic solutions show larger slip-rate amplitudes than the kinematic models. Unlike kinematic modeling, in dynamic modeling it is possible to generate high-frequency components of the source function (up to ∼5 Hz), which results in higher slip rate amplitudes compared to the lower frequency kinematic modeling (Aochi & Twardzik, 2019; Gallovič et al., 2019b). In our solution (Figure 10a), the rupture initiates roughly in the same region as in Pizzi et al. (2017): In both cases, the rupture starts NW of the hypocenter determined by (Chiaraluce et al., 2017), at shallow depths. This similarity may arise from the fact that we used a configuration similar to that of Pizzi et al. (2017) in terms of elastic properties of the medium, fault geometry and strong-motion stations. However, the nucleation in our solution is shallower than that of Pizzi et al. (2017). In addition, due to the low spatial resolution of our model, the size of the nucleation patch in our solution is larger than what was inferred by Pizzi et al. (2017). Note that in dynamic inversion methods, the nucleation was enforced to start from a prior hypocenter location. In particular, Gallovič et al. (2019b) constrained their rupture to initiate from the nucleation patch found by Pizzi et al. (2017), while Aochi and Twardzik (2019) used a two layered medium, and constrained slip to start from a different hypocenter location, determined by INGV (http://terremoti.ingv.it/en/event/7073641). Nevertheless, the two slip patches imaged SE and NW of the hypocenter by Aochi and

Figure 10. Snapshots showing the evolution of the sliprate in time, as obtained by (a) this study; (b) Pizzi et al. (2017) applying the kinematic finite-fault inversion method of Gallovič et al. (2015); (c) Gallovič et al. (2019b) by Bayesian dynamic finite-fault inversion (Gallovič et al., 2019a); and (d) Aochi and Twardzik (2019) inferred by a hybrid dynamic method. All inversions confirm the bilaterality of the rupture, the relative higher slip-rates toward the NW of the hypocenter and the weak nucleation. (a), (b) and (c) suggest a nucleation depth around 4.0 km. In (d), the hypocenter was fixed *a priori*. The rupture speed is relatively slower and the ruptured area is relatively smaller in (c), (d), which compensates for the higher slip amplitude. Dashed lines identify the area that corresponds to our modeled fault plane.

Twardzik (2019) are consistent with our solution. The differences between the nucleation locations in the finite-fault solutions, on one hand, and the independently determined hypocenters, on the other hand, could be attributed to epistemic uncertainty in the kinematic finite fault inversions. As pointed out by Ragon et al. (2018, 2019), several sources of epistemic uncertainty affect finite-fault inversions, namely the fault position, fault dip and crustal model. Ragon et al. (2019) used the sensitivity kernel of the forward equation to account for this epistemic uncertainty. The authors showed that assuming that the fault-dip angle is 45°, without accounting for fault-dip uncertainty, may shift the slip patches updip. The proposed neuro-fuzzy method could be improved in the future by taking into account such epistemic uncertainties. The epistemic uncertainty associated with fault geometry and dip complexity can affect the poor fit of some static GNSS data, particularly at SE stations (e.g., CAPI and MSNI in Figure 7). According to Lavecchia et al. (2016), who carried out sophisticated fault geometry modeling, the Amatrice causative fault consists of two segments with different dip angles. Their analysis suggests that at shallow depths (<8 km), the northeastern segment dips 50° – 60°, while the southern segment has a steeper dip angle of ~60°. The authors propose that the two surfaces converge into a continous surface at depths below 8 km and the dip angle reduces to 45°. A steeper dip angle at shallow depths can result in higher vertical surface displacements that better simulate the high vertical displacements observed at SE stations. At the current stage of development of our method, we could not account for fault plane complexities and rather assumed a simpler single segment fault plane.

Let us compare the rupture speed inferred from the neuro-fuzzy method with that inferred from the dynamic inversion models, by considering the rupture arrival contours in Figure 9. The rupture propagation speed in our model, as inferred from the rupture arrival times (Figure 9), is more similar to that of Aochi and Twardzik (2019) than to that of Gallovič et al. (2019b). Both the neuro-fuzzy model and that of Aochi and Twardzik (2019) show a rupture lasting ~4-s to SE and ~6-s to the NW. However, by considering that the large areas to the NW and SE break in less than 5 s (Figure 9c), our solution shows a faster rupture speed than that of Gallovič et al. (2019b), evidencing the trade-off between slip rate amplitudes and rupture speed in the dynamic model (Gallovič et al., 2019b). The smaller ruptured area in Gallovič et al. (2019b) can also be affected by this trade-off.

It is worth noting that in our solution the spatio-temporal resolution of the inverted slip is limited because we invert low-frequency ground motion and use only a few spatial basis functions. Because of this limited resolution, a point source is imaged as a smeared circle. Consequently, the nucleation patch can be represented as a growing circle, which could be misinterpreted as a rapidly propagating rupture. The fast rupture speed in the first second of rupture (Figure 9a) could be influenced by this limited resolution. In order to infer the rupture speed more accurately, a more accurate inversion of high-frequency ground motion is needed. Complementary studies, such as those using the back-projection method (e.g., Bao et al., 2019; Ishii et al., 2005), allow to invert the high-frequency components of ground motion and may help to better infer the rupture speed.

The dip-slip component of our source function shows similar patterns between adjacent frequencies, which indicates a well resolved solution (Figure 2). However, the patterns of the strike-slip components varies considerably between adjacent frequencies (Figure 2 and Figure S8 in the e-supplements). One possible reason for this behavior is that the strike-slip component has very low amplitudes, therefore the corresponding waveforms drop below the noise level and we are not able find a pattern of rupture that is, consistent between frequencies. If so, more observations would be needed in order to decrease the uncertainty of these model parameters. Alternatively, we could apply a constraint that would favor similar slip distributions between adjacent frequencies.

In spite of the general similarities between our slip solution and those of Aochi and Twardzik (2019); Gallovič et al. (2019b); Pizzi et al. (2017), shown here, and also those of Tinti et al. (2016); Cirella et al. (2018), not shown here, there are also some detail differences in the number and locations of asperities, rupture speeds, and slip-rate amplitudes. Such differences arise for two different reasons: (a) The model space is discretized in different ways by the various methods, which affects the singular values in the inversions. By using only a few fuzzy basis functions, in our inversion we retain only large singular values (Kheirdast et al., 2021). The solution that we obtain is robust and shows only well-constrained features, however it is a smooth solution and has a low spatial resolution. (b) The different inversions apply damping constraints with different intensities (e.g., Gallovič et al., 2019b). The effect of the damping factor (α) is shown in Figure S12 for the

static slip distribution (f = 0Hz). Here, we applied the principles of Generalized Singular Value Decomposition (GSVD), as introduced in Kheirdast et al., 2021), in order to analyze the over-determined (6×4) slip model. Figure S12a shows the image of the GNSS data on the data-space basis ($\mathbf{U}^{\mathbf{T}}_{:,i}\mathbf{d}$) versus singular values (Kheirdast et al., 2021). Let us consider five candidate α values between 0.020 (less damping) and 0.095 (high damping). The lowest value (α = 0.020) is an intersection point of the two curves shown, $\mathbf{U}^{\mathbf{T}}_{:,i}\mathbf{d}$ and γ_i, obtained from the discrete Picard condition, which states that this value ensures convergence of the inversion (Aster et al., 2018). The highest value (α = 0.095) is obtained from the maximum curvature of the L-curve. By selecting a relatively lower α, as displayed in Figures S12b and S12c two distinctive asperities can be identified. By increasing α, the inverted slip becomes more smooth and the two asperities become connected (Figure S12d–S12f). In our model, the smoothness level chosen is likely the reason why only one slip patch is observed in the static slip distribution. However, the two slip patches are independently imaged at higher frequencies, where we can clearly identify the locations that radiated the most seismic energy.

In our inversion, the regularization is frequency-dependent, therefore we apply different smoothness constraints that are specifically tuned to each frequency.

7.2. Backslip

Slip can easily be constrained to be always positive in time-domain finite fault inversions, for example, by use of non-negative LSQ algorithms (e.g., Gallovič et al., 2015). However, frequency domain formulations, as our neuro-fuzzy inversion, cannot impose slip positivity. The frequency domain formulation is a central aspect of the neuro-fuzzy inversion, which results in a simpler forward equation, that in turn allows us to use meshless fuzzy basis functions to discretize the fault plane at each frequency. Because slip positivity cannot be imposed in frequency domain finite-fault inversions, the resulting slip-rate functions may have undesired negative slip, both in the along-strike and down-dip directions (Figure 3b). These undesired ripples arise from error that affects our model, namely:

1. Inaccuracy of the forward modeling: The existing velocity-attenuation-density models and waveform modeling codes have limited accuracy (e.g., Spudich et al., 2019).
2. Bias arising from the regularization (i.e., smoothness) constraint.
3. Noise in the data, which we cannot properly account for when weighting the data due to lack of knowledge on data error.
4. Limited power of the high-frequency modeling, which in turn results in a limited power of the high-frequency reconstruction of the slip-rate function.
5. Cut-off frequency effect: The limited frequency-dependent components in a Fourier expansion result in ripples in the reconstructed signal. In order to mitigate this effect, a classical approach is to apply tapering functions to the signal's spectrum, as to avoid such ripples. In this study, we applied cosine tapers to mitigate the cut-off frequency effect.
6. Lack of transfer knowledge between adjacent frequency points, that is, we do not impose a similarity constraint between adjacent frequencies, which would result in a more physically plausible source time function, with smoother source spectra.

Nevertheless, Figure 3b shows that meaningful slip-rates can be resolved using the neuro-fuzzy inversion, even without a slip positivity constraint. In particular, backslip and spurious oscillations of the source time function are very limited when the number of fuzzy basis functions is chosen using the maximum likelihood criterion.

7.3. How to Choose an Adequate Number of Fuzzy Basis Functions?

We showed in Section 6 that a maximum likelihood approach can be used to find a number of fuzzy basis functions that is, specifically suited for each frequency. We showed that this approach results in using less fuzzy basis functions at low frequencies, where less spatial resolution in needed, and more fuzzy basis functions at high frequencies, where more fuzzy basis functions are needed in order to resolve the rupture process and fit the data well. The seismic moments inferred from the over-determined and maximum-like-

lihood approaches are, respectively, 2.22×10^{18} N.m and 2.21×10^{18} N.m, both in good agreement with the seismic scalar moment of 2.48×10^{18} N.m provided by the GCMT project (Ekstrom et al., 2012).

Although the maximum likelihood approach yields superior solutions, it is also computationally more intense than the simple over-determined approach. Hence, we recommend that the maximum likelihood approach be used whenever computational resources are not a concern and a higher quality solution is desired. The over-determined approach remains useful when computational burden is a concern or when a quick solution is needed.

7.4. Validation of the Neuro-Fuzzy Inversion Solution

When enough observations are available, it is possible to divide the entire data set into two subsets: One which will serve for training or inversion and another one that will serve for validation, a procedure that is, common in data science (e.g., Goodfellow et al., 2016). The training data set is used to determine the model parameters, whereas the validation data set is used to control the robustness of the inferred parameters. By comparing the model output with the validation data set, one can decide whether the obtained parameters are appropriate, that is, whether they can replicate the expected behavior as given by the validation data set.

Given the wealth of data available for the Amatrice earthquake, we were able to divide the data set in the strong-motion frequency range $(0.06 < f < 0.5)$Hz into two datasets: that recorded by accelerometric seismic stations and that recorded by high-rate GNSS data. As explained before, in this frequency range, our finite-fault solution was inferred from the accelerometric data only (training data set). In this section we show how well our finite-fault model predicts the GNSS waveforms, which were not used when searching for the model parameters (validation data set).

Figure 11 shows the observed high-rate GNSS velocity waveforms, together with the synthetics obtained from our preferred solution. That is, that obtained by using the maximum likelihood approach to select the adequate number of fuzzy basis functions. The comparison with synthetics obtained from the solution that uses 6×4 basis functions is shown in e-supplement (Figure S13). All waveforms are band-pass filtered in the frequency range of the inversion, that is, 0.06–0.5 Hz. The waveforms at each station-component are normalized, with the maximum amplitude of each waveform written in front of each trace. The comparison between observed and synthetic waveforms shows a very good visual match.

The maximum likelihood approach has a relatively higher reconstruction power with respect to the over-determined approach. Not only the amplitudes of the waveforms are well recovered from our slip model, but the arrival phases are also consistent, indicating that our slip model is able to consistently predict the observed high-rate GNSS records. This agreement is particularly notable given that the training and validation datasets were recorded by different types of instruments. This comparison is presented in the spectral domain in Figure S14 for the overdetermined (6×4, red-line) and maximum likelihood (blue-line) criteria, respectively.

The accuracy of the inversion results obtained from the maximum likelihood and over-determined approaches are quantitatively assessed in Table 3, using the residual norms between synthetic waveforms and validation data set (GNSS data) at each frequency. The residual norm of the validation data is composed of three fundamental quantities: The variance of the synthetic forward simulation from the observed high-rate GNSS data, the squared bias of the synthetic data due to regularization, and the inherent noise of GNSS data, the latter of which does not depend on modeling procedure. Different parameterization methods will affect the residual norm, through the trade-off between the forward simulation variance and the bias in the predicted waveforms. That is, training a less flexible system (fewer model parameters) will result in relatively more biased synthetics with smaller variance with validation (test) data, when compared to a more flexible system. Thus, in the maximum likelihood approach, increasing the number of fuzzy basis functions at higher frequencies may increase the forward simulation variance and consequently increase also the residual norm of the validation data set. In a good solution, if by increasing the number of parameters, the inverted model resembles the true model, the residual norm between the synthetic and validation data should not increase (James et al., 2013). Table 3 shows that the residual norm does not differ substan-
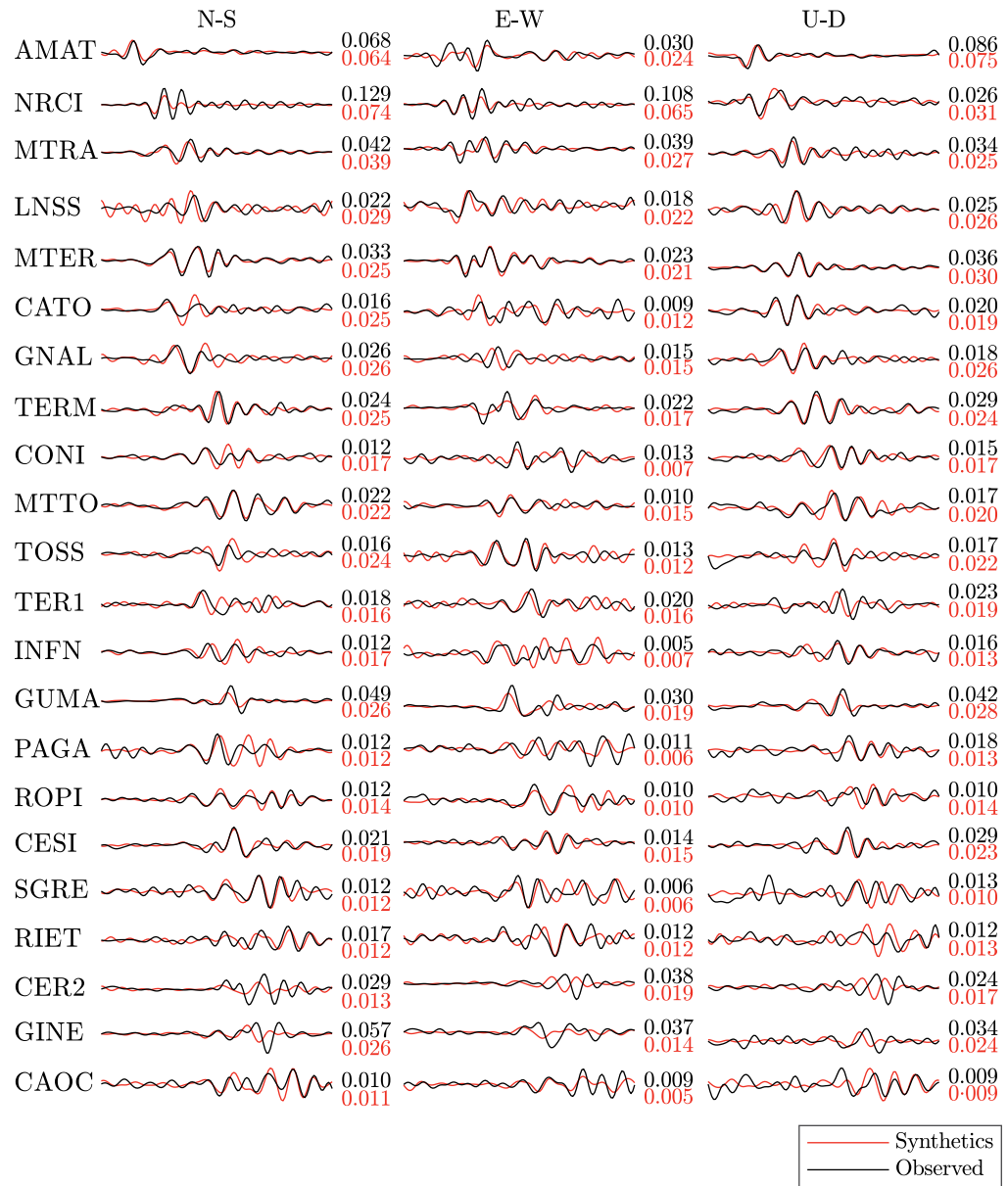
Figure 11. Validation of the slip model inferred from strong-motion data (training data set) using high-rate GNSS data as validation data set. The high-rate GNSS data was not used in the inversion, rather it is predicted from the slip model in order to assess the quality of the model. The inversion relied on the maximum likelihood approach to select the adequate number of fuzzy basis functions. For each station and component of ground motion we show synthetic (red) and observed high-rate GNSS (black) waveforms. The numbers in front of each waveform indicate their maximum amplitude.

tially depending on the discretization method. In particular, increasing the number of fuzzy basis functions does not dramatically change the residual norm of the validation data and the validation residual norms of the over-determined and maximum likelihood methods are almost equal. Therefore, by increasing the number of basis functions, the maximum likelihood solution does not overfit data set, because the residual norms of the validation data do not substantially increased.

The residual norm between synthetic and validation data increases with increasing frequency (Table 3), thus implying that modeling uncertainty is relatively higher at high frequencies. These uncertainty values may be used to decide on the reliable range of solution frequencies. For example, one can compares the value of the validation residual norms with the probability distribution of the measured noise at HR-

GNSS stations and select the range of frequencies for which the validation norm represents an acceptable noise likelihood. Note that the spatial slip resolution is reduced with increasing frequency (Olson & Anderson, 1988), therefore small scale slip variations at high frequencies may not be reliable. In the interpretation of frequency-dependent slip models, the most reliable parts of the model are slip patches that can be identified persistently at adjacent frequencies. A localized slip patch in a single frequency is likely to correspond to an artifact of the inversion.

8. Conclusion

In this article we validated the neuro-fuzzy kinematic finite-fault inversion method (Kheirdast et al., 2021) by applying it to data of the Mw6.2, Aug/24/2016 Amatrice earthquake. The Amatrice earthquake was extremely well recorded in the near field by a dense network of strong-motion and high-rate GNSS instruments. We implemented two different approaches to determine the adequate number of fuzzy basis functions: (a) Ensuring that the ratio between the number of model parameters and the number of observations is such that the inverse problem is formally over-determined (Section 4); and (b) Using a maximum likelihood approach to select an adequate number of basis functions at each frequency (Section 6). Both methods reveal the same general features of the earthquake rupture, which agree well with previous studies (Aochi & Twardzik, 2019; Gallovič et al., 2019b; Pizzi et al., 2017) (Section 7.1). Nevertheless, the maximum likelihood approach correctly identifies that more basis functions are needed at high frequencies in order to properly describe the rupture process, hence achieving a more detailed slip model and improved data fit. The inferred slip model shares several similarities with previous dynamic solutions, namely concerning the spatial slip distribution, rise time and rupture arrival time. However, the well-imaged nucleation patch suggested by previous studies is not obtained in our kinematic solution and the size of the ruptured area in our solution is larger than in dynamic inversions. We validated our final slip model by using it to predict the ground motion recorded at high-rate GNSS stations, not used in the inversion, in the frequency range 0.06–0.5 Hz. The fit between the GNSS data not used in the inversion and the synthetics generated by our slip model was excellent, revealing the high quality of the retrieved solution. Our source model shows a slow nucleation stage (~2 sec), followed by a bilateral rupture to the NW and SE of the hypocenter, with higher slip amplitude to the NW.

Data Availability Statement

The work presented here was performed with data provided by the Rete Accelerometrica Nazionale operated by the Italian Department of Civil Protection and the Rete Sismometrica Nazionale operated by the Istituto Nazionale di Geofisica e Vulcanologia. The records are available online (https://esm.mi.ingv.it/). The authors downloaded the seismic data from the Engineering Strong-Motion database (Luzi, Puglia, Russo, D'Amico, et al., 2016; Luzi, Puglia, Russo, & ORFEUS WG5, 2016). Static and high-rate GNSS data was processed by Cheloni et al. (2017) and Avallone et al. (2016), respectively. The processed HR-GNSS recordings, as the authors adopted from Avallone et al. (2016), are available online at https://doi.org/10.5281/zenodo.5040186. Corrected static GNSS data can be accessed from Cheloni et al. (2017). The finite-fault solution of Pizzi et al. (2017) was downloaded from SRCMOD (online database of finite-fault rupture models of past earthquakes) website (http://equake-rc.info/srcmod/) (Mai & Thingbaijam, 2014).

References

Ameri, G., Gallovič, F., & Pacor, F. (2012). Complexity of the mw 6.3 2009 l'aquila (Central Italy) earthquake: 2. broadband strong motion modeling. *Journal of Geophysical Research*, *117*(B4). https://doi.org/10.1029/2011jb008729

Aochi, H., & Twardzik, C. (2019). Imaging of seismogenic asperities of the 2016 ml 6.0 amatrice, Central Italy, earthquake through dynamic rupture simulations. *Pure and Applied Geophysics*, *177*, 1931–1946. https://doi.org/10.1007/s00024-019-02199-z

Aster, R. C., Borchers, B., & Thurber, C. H. (2018). *Parameter estimation and inverse problems*. Elsevier.

Avallone, A., Latorre, D., Serpelloni, E., Cavaliere, A., Herrero, A., Cecere, G., et al. (2016). Coseismic displacement waveforms for the 2016 august 24 mw 6.0 amatrice earthquake (Central Italy) carried out from high-rate gps data. *Annals of Geophysics*, *59*. https://doi.org/10.4401/ag-7275

Avallone, A., Selvaggi, G., D'Anastasio, E., D'Agostino, N., Pietrantonio, G., Riguzzi, F., & Zarrilli, L. (2010). The ring network: Improvement of a gps velocity field in the central mediterranean. *Annals of Geophysics*, *53*(2), 39–54. https://doi.org/10.4401/ag-4549

Bao, H., Ampuero, J.-P., Meng, L., Fielding, E. J., Liang, C., Milliner, C. W. D., et al. (2019). Early and persistent supershear rupture of the 2018 magnitude 7.5 palu earthquake. *Nature Geoscience*, *12*(3), 200–205. https://doi.org/10.1038/s41561-018-0297-z

Bernard, P., Herrero, A., & Berge, C. (1996). Modeling directivity of heterogeneous earthquake ruptures. *Bulletin of the Seismological Society of America*, *86*(4), 1149–1160.

Bertiger, W., Desai, S. D., Haines, B., Harvey, N., Moore, A. W., Owen, S., & Weiss, J. P. (2010). Single receiver phase ambiguity resolution with gps data. *Journal of Geodesy*, *84*(5), 327–337. https://doi.org/10.1007/s00190-010-0371-9

Bouchon, M. (2003). A review of the discrete wavenumber method. *Pure and Applied Geophysics*, *160*(3), 445–465. https://doi.org/10.1007/PL00012545

Casarotti, E., Magnoni, F., Faenza, L., Comunello, F., Polidoro, P., & Mulargia, S. (2016). Fast 3d seismic wave simulations of August 24, 2016 mw 6.0 Central Italy earthquake for visual communication. *Annals of Geophysics*, *59*. https://doi.org/10.4401/ag-7231

Cheloni, D., De Novellis, V., Albano, M., Antonioli, A., Anzidei, M., Atzori, S., et al. (2017). Geodetic model of the 2016 Central Italy earthquake sequence inferred from insar and gps data. *Geophysical Research Letters*, *44*(13), 6778–6787. https://doi.org/10.1002/2017gl073580

Cheloni, D., Serpelloni, E., Devoti, R., D'Agostino, N., Pietrantonio, G., Riguzzi, F., et al. (2016). Gps observations of coseismic deformation following the 2016, August 24, mw 6 amatrice earthquake (Central Italy): Data, analysis and preliminary fault model. *Annals of Geophysics*, *59*. https://doi.org/10.4401/ag-7269

Chiaraluce, L., Di Stefano, R., Tinti, E., Scognamiglio, L., Michele, M., Casarotti, E., et al. (2017). The 2016 Central Italy seismic sequence: A first look at the mainshocks, aftershocks, and source models. *Seismological Research Letters*, *88*(3), 757–771. https://doi.org/10.1785/0220160221

Cirella, A., Pezzo, G., & Piatanesi, A. (2018). Rupture kinematics and structural-rheological control of the 2016 mw6.1 Amatrice (Central Italy) earthquake from joint inversion of seismic and geodetic data. *Geophysical Research Letters*, *45*(22), 12302–12311. https://doi.org/10.1029/2018gl080894

Cotton, F., & Campillo, M. (1995). Frequency domain inversion of strong motions: Application to the 1992 landers earthquake. *Journal of Geophysical Research*, *100*(B3), 3961–3975. https://doi.org/10.1029/94jb02121

Coutant, O. (1989). *Program of numerical simulation axitra*. Universite Joseph Fourier.

Coutant, O. (2020). Coutanto/axitra: axitra v2019. Zenodo. https://doi.org/10.5281/zenodo.3985053

Das, S., & Kostrov, B. V., (1990). Inversion for seismic slip rate history and distribution with stabilizing constraints: Application to the 1986 Andreanof Islands earthquake. *Journal of Geophysical Research*, *95*(B5), 6899–6913. https://doi.org/10.1029/JB095iB05p06899

Ekstrom, G., Nettles, M., & Dziewoński, A. (2012). The global cmt project 2004–2010: Centroid-moment tensors for 13,017 earthquakes. *Physics of the Earth and Planetary Interiors*, *200–201*, 1–9. https://doi.org/10.1016/j.pepi.2012.04.002

Fan, W., Shearer, P. M., & Gerstoft, P. (2014). Kinematic earthquake rupture inversion in the frequency domain. *Geophysical Journal International*, *199*(2), 1138–1160. https://doi.org/10.1093/gji/ggu319

Gallovič, F. (2006). *Kinematic modeling of strong ground motions*.

Gallovič, F., & Ampuero, J.-P. (2015). A new strategy to compare inverted rupture models exploiting the eigenstructure of the inverse problem. *Seismological Research Letters*, *86*(6), 1679–1689.

Gallovič, F., & Brokešová, J. (2004). On strong ground motion synthesis with k- 2 slip distributions. *Journal of Seismology*, *8*(2), 211–224.

Gallovič, F., Imperatori, W., & Mai, P. M. (2015). Effects of three-dimensional crustal structure and smoothing constraint on earthquake slip inversions: Case study of the mw6.3 2009 l'aquila earthquake. *Journal of Geophysical Research: Solid Earth*, *120*(1), 428–449. https://doi.org/10.1002/2014JB011650

Gallovič, F., Valentová, L., Ampuero, J.-P., & Gabriel, A.-A. (2019a). Bayesian dynamic finite-fault inversion: 1. method and synthetic test. *Journal of Geophysical Research: Solid Earth*, *124*(7), 6949–6969. https://doi.org/10.1029/2019JB017510

Gallovič, F., Valentová, L., Ampuero, J.-P., & Gabriel, A.-A. (2019b). Bayesian dynamic finite-fault inversion: 2. application to the 2016 mw 6.2 Amatrice, Italy, earthquake. *Journal of Geophysical Research: Solid Earth*, *124*(7), 6970–6988. https://doi.org/10.1029/2019JB017512

Gallovič, F., & Zahradník, J. (2011). Toward understanding slip inversion uncertainty and artifacts: 2. singular value analysis. *Journal of Geophysical Research*, *116*(B2).

Galvani, A., Anzidei, M., Devoti, R., Esposito, A., Pietrantonio, G., Pisani, A. R., et al. (2013). The interseismic velocity field of the Central Apennines from a dense GPS network. *Annals of Geophysics*, *55*(5). https://doi.org/10.4401/ag-5634

Goodfellow, I., Bengio, Y., & Courville, A. (2016). *Deep learning*. MIT Press. http://www.deeplearningbook.org

Hansen, P. C. (2005). *Rank-deficient and discrete ill-posed problems*. Siam.

Hartzell, S. H., & Heaton, T. H. (1983). Inversion of strong ground motion and teleseismic waveform data for the fault rupture history of the 1979 Imperial Valley, California, earthquake. *Bulletin of the Seismological Society of America*, *12*(6A), 1553–1583. https://doi.org/10.1785/bssa07306a1553

Herring, T., King, R., & McClusky, S. (2010). *Gamit Reference Manual release 10.4*. Massachusetts Institute of Technology.

Huang, M.-H., Fielding, E. J., Liang, C., Milillo, P., Bekaert, D., Dreger, D., & Salzer, J. (2017). Coseismic deformation and triggered landslides of the 2016 mw 6.2 amatrice earthquake in Italy. *Geophysical Research Letters*, *44*(3), 1266–1274. https://doi.org/10.1002/2016gl071687

Ide, S. (2015). 4.09 - Slip inversion. In G. Schubert (Ed.), *Treatise on geophysics* (2nd ed., pp. 215–241). Elsevier. https://doi.org/10.1016/b978-0-444-53802-4.00076-2

INGV Ring Working Group and others. (2016). Rete integrata nazionale gps. https://doi.org/10.13127/RING

INGV Seismological Data Centre. (1997). *Rete sismica nazionale (rsn). Istituto Nazionale di Geofisica e Vulcanologia (INGV), Italy*. https://doi.org/10.13127/SD/X0FXNH7QFY

Ishii, M., Shearer, P. M., Houston, H., & Vidale, J. E. (2005). Extent, duration and speed of the 2004 sumatra–andaman earthquake imaged by the hi-net array. *Nature*, *435*(7044), 933–936. https://doi.org/10.1038/nature03675

James, G., Witten, D., Hastie, T., & Tibshirani, R. (2013). *An Introduction to Statistical Learning* (Vol. 112). Springer.

Kheixrdast, N., Ansari, A., & Custôdio, S. (2021). Fuzzy kinematic finite-fault inversion: 1. Theory and synthetic test. *Journal of Geophysical Research: Solid Earth*, e2020JB020770.

Lavecchia, G., Castaldo, R., de Nardis, R., De Novellis, V., Ferrarini, F., Pepe, S., & Tizzani, P. (2016). Ground deformation and source geometry of the 24 august 2016 amatrice earthquake (Central Italy) investigated through analytical and numerical modeling of dinsar measurements and structural-geological data. *Geophysical Research Letters*, *43*(24), 389–12. https://doi.org/10.1002/2016gl071723

Liu, P., & Archuleta, R. J. (2004). A new nonlinear finite fault inversion with three-dimensional green's functions: Application to the 1989 loma prieta, California, earthquake. *Journal of Geophysical Research: Solid Earth*, *109*(B2). https://doi.org/10.1029/2003jb002625

Luzi, L., Puglia, R., Russo, E., D'Amico, M., Felicetta, C., Pacor, F., et al. (2016). The engineering strong-motion database: A platform to access pan-european accelerometric data. *Seismological Research Letters*, *87*(4), 987–997. https://doi.org/10.1785/0220150278

Luzi, L., Puglia, R., Russo, E., ORFEUS, W. G. 5., Felicetta, C., Pacor, F., et al. (2016). Engineering strong motion database, version 1.0. Istituto Nazionale di Geofisica e Vulcanologia. *Observatories & Research Facilities for European Seismology*, *10*, 987–997. https://doi.org/10.1785/0220150278

Mai, P. M., Schorlemmer, D., Page, M., Ampuero, J.-P., Asano, K., Causse, M., Custodio, S., et al. (2016). The earthquake-source inversion validation (siv) project. *Seismological Research Letters*, *87*(3), 690–708. https://doi.org/10.1785/0220150231

Mai, P. M., & Thingbaijam, K. K. S. (2014). SRCMOD: An online database of finite-fault rupture models. *Seismological Research Letters*, *85*(6), 1348–1357. https://doi.org/10.1785/0220140077

Magnoni, F., & Casarotti, E., (2016). Kinematic finite fault and 3d seismic wave propagation of the 24 august, 2016, mw 6.0 Central Italy earthquake. *Annals of Geophysics*, *59*. https://doi.org/10.4401/ag-7265

Olson, A. H., & Anderson, J. G. (1988). Implications of frequency-domain inversion of earthquake ground motions for resolving the space-time dependence of slip on an extended fault. *Geophysical Journal International*, *94*(3), 443–455. https://doi.org/10.1111/j.1365-246X.1988.tb02267.x

Olson, A. H., & Apsel, R. J. (1982). Finite faults and inverse theory with applications to the 1979 Imperial Valley earthquake. *Bulletin of the Seismological Society of America*, *12*(6A), 1969–2001. https://doi.org/10.1785/bssa07206a1969

Pizzi, A., Di Domenica, A., Gallovič, F., Luzi, L., & Puglia, R. (2017). Fault segmentation as constraint to the occurrence of the main shocks of the 2016 Central Italy seismic sequence. *Tectonics*, *36*(11), 2370–2387. https://doi.org/10.1002/2017tc004652

Presidency Of Counsil Of Ministers - Civil Protection Department. (1972). Italian strong motion network. *Presidency of Counsil of Ministers - Civil Protection Department*. https://doi.org/10.7914/SN/IT

Ragon, T., Sladen, A., & Simons, M. (2018). Accounting for uncertain fault geometry in earthquake source inversions – I: Theory and simplified application. *Geophysical Journal International*, *214*(2), 1174–1190. https://doi.org/10.1093/gji/ggy187

Ragon, T., Sladen, A., & Simons, M. (2019). Accounting for uncertain fault geometry in earthquake source inversions – II: Application to the Mw 6.2 Amatrice earthquake, central Italy. *Geophysical Journal International*, *218*(1), 689–707. https://doi.org/10.1093/gji/ggz180

Scognamiglio, L., Tinti, E., Casarotti, E., Pucci, S., Villani, F., Cocco, M., et al. (2018). Complex fault geometry and rupture dynamics of the mw 6.5, 30 October 2016, Central Italy earthquake. *Journal of Geophysical Research: Solid Earth*, *123*(4), 2943–2964. https://doi.org/10.1002/2018jb015603

Serpelloni, E., Anderlini, L., Avallone, A., Cannelli, V., Cavaliere, A., Cheloni, E., et al. (2012). Gps observations of coseismic deformation following the May 20 and 29, 2012, Emilia Seismic Events (Northern Italy): Data, analysis and preliminary models. *Annals of Geophysics*, *55*(4). https://doi.org/10.4401/ag-6168

Sokos, E., & Zahradník, J. (2013). Evaluating centroid-moment-tensor uncertainty in the new version of ISOLA software. *Seismological Research Letters*, *84*(4), 656–665. https://doi.org/10.1785/0220130002

Somala, S. N., Ampuero, J.-P., & Lapusta, N. (2018). Finite-fault source inversion using adjoint methods in 3-D heterogeneous media. *Geophysical Journal International*, *214*(1), 402–420. https://doi.org/10.1093/gji/ggy148

Spudich, P., Cirella, A., Scognamiglio, L., & Tinti, E. (2019). Variability in synthetic earthquake ground motions caused by source variability and errors in wave propagation models. *Geophysical Journal International*, *219*(1), 346–372. https://doi.org/10.1093/gji/ggz275

Tinti, E., Scognamiglio, L., Michelini, A., & Cocco, M. (2016). Slip heterogeneity and directivity of the ml 6.0, 2016, amatrice earthquake estimated with rapid finite-fault inversion. *Geophysical Research Letters*, *43*(20), 745–10. https://doi.org/10.1002/2016gl071263

Tung, S., & Masterlark, T. (2018). Resolving source geometry of the 24 August 2016 Amatrice, Central Italy, Earthquake from InSAR data and 3D finite-element modeling. *Bulletin of the Seismological Society of America*, *108*(2), 553–572. https://doi.org/10.1785/0120170139

Walters, R., Gregory, L., Wedmore, L., Craig, T., McCaffrey, K., Wilkinson, M., et al. (2018). Dual control of fault intersections on stop-start rupture in the 2016 Central Italy seismic sequence. *Earth and Planetary Science Letters*, *500*, 1–14. https://doi.org/10.1016/j.epsl.2018.07.043

Wessel, P., Luis, J. F., Uieda, L., Scharroo, R., Wobbe, F., Smith, W. H. F., & Tian, D. (2019). The generic mapping tools version 6. *Geochemistry, Geophysics, Geosystems*, *20*(11), 5556–5564. https://doi.org/10.1029/2019gc008515

Zumberge, J., Heflin, M., Jefferson, D., Watkins, M., & Webb, F. (1997). Precise point positioning for the efficient and robust analysis of gps data from large networks. *Journal of Geophysical Research: solid earth*, *102*(B3), 5005–5017. https://doi.org/10.1029/96jb03860